Global optical model potential for $A = 3$ projectiles

D. Y. Pang
GANIL, CEA/DSM-CNRS/IN2P3, Boulevard Henri Becquerel, Boîte Postale 55027, F-14076 Caen Cedex 5, France and School of Physics and State Key Laboratory of Nuclear Physics and Technology, Peking University, Beijing, People's Republic of China

P. Roussel-Chomaz* and H. Savajols
GANIL, CEA/DSM-CNRS/IN2P3, Boulevard Henri Becquerel, Boîte Postale 55027, F-14076 Caen Cedex 5, France

R. L. Varner
Physics Division, Oak Ridge National Laboratory, Oak Ridge, Tennessee 37831, USA

R. Wolski
JINR, FLNR, RU-141980 Dubna, Russia and The Henryk Niewodniczański Institute of Nuclear Physics, Krakow, Poland
(Received 13 November 2008; published 25 February 2009)

A global optical model potential (GDP08) for ^{3}He projectiles has been obtained by simultaneously fitting the elastic scattering data of ^{3}He from targets of $40 \leqslant A_T \leqslant 209$ at incident energies of $30 \leqslant E_{\rm inc} \leqslant 217$ MeV. Uncertainties and correlation coefficients between the global potential parameters were obtained by using the bootstrap statistical method. GDP08 was found to satisfactorily account for the elastic scattering of ^{3}H as well, which makes it a global optical potential for the $A = 3$ nuclei. Optical model calculations using the GDP08 global potential are compared with the experimental angular distributions of differential cross sections for ^{3}He-nucleus and ^{3}H-nucleus scattering from different targets of $6 \leqslant A_T \leqslant 232$ at incident energies of $4 \leqslant E_{\rm inc} \leqslant 450$ MeV. The optical potential for the doubly-magic nucleus ^{40}Ca, the low-energy correction to the real potential for nuclei with $58 \lesssim A_T \lesssim 120$ at $E_{\rm inc} < 30$ MeV, the comparison with double-folding model calculations and the CH89 potential, and the spin-orbit potential parameters are discussed.

DOI: 10.1103/PhysRevC.79.024615 PACS number(s): 24.10.Ht, 25.10.+s, 25.55.Ci, 27.10.+h

I. INTRODUCTION

During the past four decades the optical model has been extensively used in the analysis of elastic and inelastic scattering of pions, nucleons, and heavier particles by nuclei over a wide range of energies [1]. Optical model potentials (OMPs), which are supposed to account for the elastic scattering of the projectile-target system, are widely used to generate the distorted waves used to analyze the cross sections of many reactions, and these analyses have proved to be a powerful tool to extract nuclear structure information [2–4].

One of the great strengths of the optical model is that it is possible to fit elastic scattering by many nuclei over a range of energies with parameters that vary smoothly with A, Z, and incident energy. This makes it possible to obtain global potentials that are very useful in reaction analysis since distorted waves are often required for energies and target nuclei for which no elastic scattering measurements are available. Global potentials are also important in large-scale calculations [5,6], in which it is very difficult to obtain optical potentials by individual fitting of elastic scattering data, even if the experimental data needed exist. Global potentials for nucleons ($A = 1$) [7–11] and deuterons ($A = 2$) [12,13] have been developed by different authors. However, despite sustained efforts [14–18], there is no satisfactory global potential for the $A = 3$ nuclei, namely, ^{3}He and ^{3}H, that is suitable for a large enough range of targets and incident energies.

The measurements performed during the past forty years form a database of angular distributions of elastic scattering differential cross sections and polarization data of ^{3}He and ^{3}H nuclei that covers a large range of target masses and incident energies. This makes the quest for a systematic optical potential for $A = 3$ nuclei possible. The computer code MINOPT [8], a combination of the optical model program OPTICS [19] and the well-known parameter minimization program MINUIT [20], was successfully used to develop the CH89 nucleon-nucleus systematic potential. We have used it to simultaneously fit 106 sets (4578 data points in total) of ^{3}He elastic scattering cross-section angular distributions from targets with $40 \leqslant A_T \leqslant 209$ and incident energies of $30 \leqslant E_{\rm inc} \leqslant 217$ MeV with 15 parameters. The resulting global potential, GDP08, was found to satisfactorily reproduce the elastic scattering data of both ^{3}He and ^{3}H nuclei. As a test and application of GDP08 in direct nuclear reactions, Lee *et al.* [21] show that ground-state proton spectroscopic factors extracted by comparing to distorted-wave Born approximation (DWBA) calculations using GDP08 with the experimental data of the (^{3}He,d) reaction in Ref. [22] are in reasonable agreement with the values predicted by large-basis shell-model calculations using the computer code OXBASH [23].

The GDP08 parametrization, guided by double-folding calculations and previous work of CH89, is discussed in

*Corresponding author: patricia.chomaz@ganil.fr

Sec. II. In Sec. III we show the database used in the present analysis. The optimal parameter values of GDP08 and its comparison with elastic scattering and reaction cross-section data are shown in Sec. IV. Section V is dedicated to discussion, and conclusions of the present work are given in Sec. VI.

II. PARAMETRIZATION OF THE GLOBAL POTENTIAL

A. Form of the optical model potential

The phenomenological optical model potential is defined as

$$\begin{aligned} U(r) = & -V_r f_{\rm ws}(r, R_0, a_0) - i W_v f_{\rm ws}(r, R_w, a_w) \\ & - i W_s(-4a_w)\frac{d}{dr} f_{\rm ws}(r, R_w, a_w) \\ & - 2(V_{\rm so} + i W_{\rm so})\left(\frac{-1}{r}\frac{d}{dr} f_{\rm ws}(r, R_{\rm so}, a_{\rm so})\vec{l}\cdot\vec{\sigma}\right) + V_C, \end{aligned} \tag{1}$$

where

(i) V_r, W_v, and W_s are depths of the real, volume-imaginary, and surface-imaginary parts, respectively, of the central potential;

(ii) $V_{\rm so}$ and $W_{\rm so}$ are the real and imaginary part of the spin-orbit potential;

(iii) V_C is the Coulomb potential given by

$$V_C(r) = \begin{cases} \frac{Z_P Z_T e^2}{r} & (r \geqslant R_C), \\ \frac{Z_P Z_T e^2}{2R_C}\left(3 - \frac{r^2}{R_C^2}\right) & (r \leqslant R_C), \end{cases} \tag{2}$$

where Z_P and Z_T are charge numbers of the projectile and targets nuclei, respectively, and R_C is the Coulomb radius of the target nuclei; and

(iv) $f_{\rm ws}$ is the Woods-Saxon form factor,

$$f_{\rm ws}(r, R, a) = \frac{1}{1 + \exp{(r - R)/a}}, \tag{3}$$

with R and a being the radius and diffuseness parameters of the potential. V_r, W_v, W_s, $V_{\rm so}$, and $W_{\rm so}$ have their corresponding R and a values, distinguished by their subscripts as is shown in Eq. (1).

B. Guidance from the double-folding calculations

The double-folding potential (DFP) is the superposition of the nucleon-nucleon interaction between nucleons of the projectile and their counterparts of the target nuclei with their nuclear density distributions:

$$V_{\rm DF}(E, \vec{r}) = \int \rho_1(\vec{r}_1)\rho_2(\vec{r}_2) v_{12}(\rho, E, \vec{s}) d\vec{r}_1 d\vec{r}_2, \tag{4}$$

where ρ_1 and ρ_2 are density distributions of the projectile and the target nuclei, respectively, v_{12} is the effective nucleon-nucleon interaction, which can have energy and density dependence, and $\vec{s} = \vec{r}_2 - \vec{r}_1 + \vec{r}$ with $\vec{r}$ being the distance between the center of mass of the projectile and target nuclei. The double-folding model that accounts for the density dependence of the NN interaction and properly treats nonlocal exchange effects [24] has been shown to account well for the real part of the nucleus-nucleus optical potential when using a modern effective interaction such as CDM3Y6 [25]. It is thus meaningful to use the double-folding model as a guide for the parametrization of the real part of the global OMP, such as its form of energy and target-mass dependencies. Double-folding model calculations of the ^{3}He-nucleus potentials were performed using the computer program DFPD2 [26] with the CDM3Y6 nucleon-nucleon interaction. The nuclear density distribution of ^{3}He was taken to be of Gaussian form [27]:

$$\rho(r) = c e^{-\alpha r^2}, \tag{5}$$

with $c = 0.20816\ {\rm fm}^{-3}$ and $\alpha = 0.53047\ {\rm fm}^{-2}$; these parameters correspond to a root-mean-square (RMS) radius of ^{3}He of 1.68 fm. The nuclear density distributions of the target nuclei were calculated by using a Hartree-Fock program based on the Skyrme parametrization [28].

The real part of the optical model potential is most commonly parametrized with a Woods-Saxon (WS) form:

$$V(r) = \frac{V_0}{1 + \exp[(r - R)/a]}, \tag{6}$$

where V_0, R, and a are depth, radius, and diffuseness of the WS potential. Since the purpose here is to use the DFP as a guide for the energy and mass dependence of the global potential, we take the DFP at $r = 0$, $V_{\rm DF}^{(0)}$, as the WS potential depth V_0; that is,

$$V_{\rm DF}^{(0)} \approx \frac{V_0}{1 + \exp(-R/a)} \approx V_0,$$

although they are not exactly the same when we are fitting $V_{\rm DF}(r)$ using the function in Eq. (6).

Another important quantity in the study of optical potentials is the volume integral of the potential (denoted as J_V and J_W for the real and imaginary parts of the potential, respectively):

$$\begin{aligned} J_V(E) &= \frac{1}{A_P A_T}\int V(E, \vec{r}) d\vec{r}, \\ J_W(E) &= J_{WV}(E) + J_{WS}(E) \\ &= \frac{1}{A_P A_T}\int [W_v(E, \vec{r}) + W_s(E, \vec{r})] d\vec{r} \end{aligned} \tag{7}$$

where A_P and A_T are mass numbers of the projectile and target, respectively. J_V and J_W are supposed to be independent of the projectile and target and are therefore useful to compare different optical potentials for different nuclei.

1. Energy and mass dependence of the double-folding potential

The DFP of the ^{3}He projectile at 20, 40, 100, 200, and 400 MeV with different targets of $6 \leqslant A_T \leqslant 208$ were calculated to study the mass dependence of $V_{\rm DF}^{(0)}$ and J_V. The results are shown in Fig. 1. One can see that, for the same incident energy, these two quantities depend strongly on A_T when $A_T \leqslant 40$ and tend to be a constant for heavier targets. Figure 2 shows the energy dependence of $V_{\rm DF}^{(0)}$ and J_V for the ^{12}C, ^{58}Ni, and ^{208}Pb targets from 10 to 450 MeV. This result suggests a

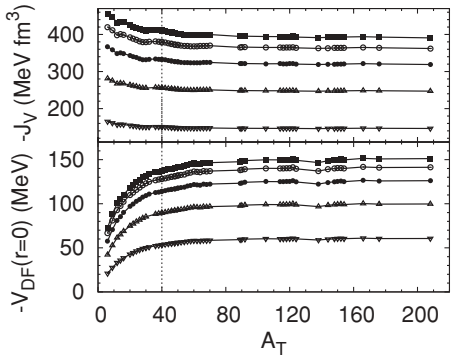

FIG. 1. Mass dependence of the depth ($V_{\rm DF}^{(0)}$) and volume integral (J_V) of the DFP for ^{3}He. Energies of ^{3}He, from top to bottom, are 20, 40, 100, 200, and 400 MeV.

linear function would be a fair approximation for the energy dependence of the real part of a global potential for ^{3}He.

2. The isospin asymmetry term of the real potential

The isospin asymmetry terms in the global optical model potential [see Eq. (12)] are important for extrapolating the potential to nuclei that are far away from the valley of stability. Figure 3 shows $V_{\rm DF}^{(0)}$ and J_V of the DFP for ^{3}He with the Ni, Sn, and Pb isotopes with different $\varepsilon = (N_T - Z_T)/A_T$ values at an incident energy of 100 MeV. One can see that the DFP for these isotopes shows a weak dependence on target isospin, which is mixed with a strong A dependence. In practice we found that the isospin asymmetry term of the real potential is not well determined by experimental data. We thus do not include the isospin asymmetry term for the real potential in the GDP08 parametrization.

C. Global parameters of the GDP08 potential

The parametrization of the present global optical potential for the $A = 3$ projectiles, GDP08, is taken from the global nucleon-nucleus potential CH89 with the guidance of double-folding calculations. Since we are using the same program that produced the CH89 global nucleon-nucleus potential,

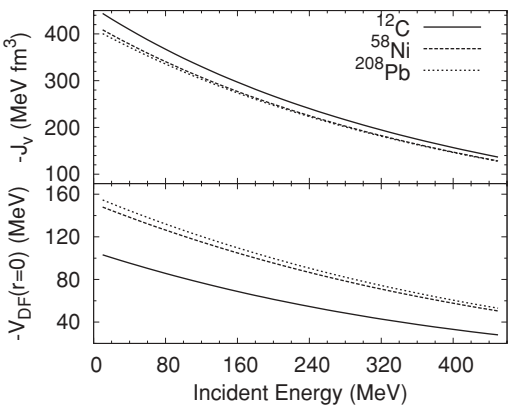

FIG. 2. Energy dependence of the depth ($V_{\rm DF}^{(0)}$) and volume integral (J_V) of the DFP for ^{3}He and ^{12}C, ^{58}Ni, and ^{208}Pb targets.

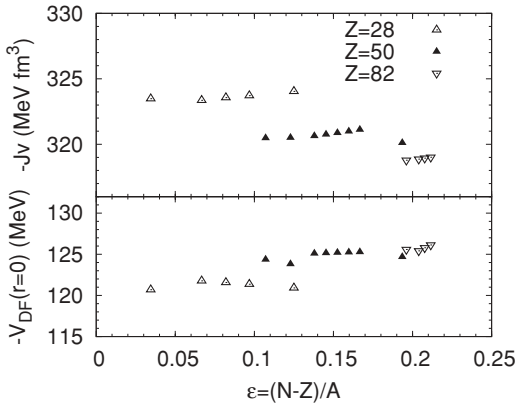

FIG. 3. Target isospin dependence of the DFP of ^{3}He with the Ni, Sn, and Pb isotopes at incident energy of 100 MeV.

it is natural to use a similar parametrization for global potential of helions and tritons. Moreover, this allows one to directly compare the resulting global potential for these $A = 3$ projectiles with the CH89 potential. The differences may reveal some information about the projectile structure effects on optical model potentials. More information on these parameters are in Ref. [8]. Note that all energies quoted in the text, or in the equations, are laboratory energies.

1. The real central potential

Taking into account the guidance of the folding model calculations, we find that the real central potential will be adequately parametrized with a linear energy dependence and no isovector dependence:

$$V_r = V_0 + V_e(E - E_C), \tag{8}$$

where E_C, the Coulomb correction to the incident energy, is

$$E_C = \alpha \frac{6 Z_P Z_T e^2}{5 R_C} \tag{9}$$

in which α was found to be unity in CH89 and the Coulomb radius was fixed to be

$$R_C = r_c A_T^{1/3} + r_c^{(0)}, \tag{10}$$

with $r_c = 1.24$ fm and $r_c^{(0)} = 0.12$ fm. In CH89, these parameters were determined by least-square fitting of the accurately determined two-parameter Fermi charge densities from electron scattering from nuclei in the mass range $40 \leqslant A_T \leqslant 209$. We use the same function for R_C for the ^{3}He-nucleus scattering.

The Coulomb correction to the incident energies is introduced to account for the energy-dependent and charge-independent nature of nuclear forces. It ensures that we evaluate the nuclear potential of the ^{3}He and ^{3}H projectiles at the same effective incident energy on a target. Failure to account for this in an energy-dependent potential will introduce spurious effects on isospin-dependent parts of the potential. The form of the Coulomb correction in Eq. (8) has been used in studies of global nucleon-nucleus potentials (e.g., Refs. [9,29]). Note that Eq. (9) is equivalent to a $Z_T A_T^{-1/3}$ term

in the real potential that has been introduced in previous work such as Refs. [17,30].

The radius of the central real potential consists of a term that is proportional to $A_T^{1/3}$ and an offset term:

$$R_0 = r_0 A_T^{1/3} + r_0^{(0)}. \tag{11}$$

The diffuseness parameter a_0 was assumed to have no dependence on either A_T or E.

2. The absorptive central potential

The depth of the imaginary potential is parametrized as

$$\begin{aligned} W(E,r) &= W_v(E) f_{\rm ws}(r, R_{\rm wv}, a_{\rm wv}) + W_s(E) f_{\rm ws}(r, R_{\rm ws}, a_{\rm ws}) \\ &= \frac{W_{\rm v0}}{1+\exp\left(\frac{W_{\rm ve0}-(E-E_C)}{W_{\rm vew}}\right)} f_{\rm ws}(r, R_{\rm wv}, a_{\rm wv}) \\ &\quad + \frac{(W_{\rm s0} \pm W_{\rm st}\varepsilon)}{1+\exp\left(\frac{(E-E_C)-W_{\rm se0}}{W_{\rm sew}}\right)} f_{\rm ws}(r, R_{\rm ws}, a_{\rm ws}), \end{aligned} \tag{12}$$

where $\varepsilon = (N_T - Z_T)/A_T$ is the isospin asymmetry of the target nucleus, the $+$ and $-$ signs are for (^{3}He,^{3}He) and (^{3}H,^{3}H) scattering, respectively, and W_v and W_s, as functions of incident energy, are depths of the volume and surface imaginary potentials, respectively. This form of energy dependence satisfies the criterion of smoothness of the volume integral of the imaginary potential in E. In CH89, W_v was assumed to be isoscalar for consistency with results from medium-energy proton scattering. We make the same assumption here.

The volume and surface imaginary potentials were assumed to have the same geometry parameters:

$$R_{\rm wv} \equiv R_{\rm ws} = R_w = r_w A_T^{1/3} + r_w^{(0)}, \tag{13}$$

and, analogous to that of the real potential, the diffuseness parameters $a_{\rm wv} \equiv a_{\rm ws} = a_w$ were assumed to be independent of A_T and E.

3. The spin-orbit potential

The spin-orbit potential is parametrized as

$$V_{\rm so} = V_{\rm so0} + V_{\rm soe} E, \tag{14}$$

and its geometry parameters are

$$R_{\rm so} = r_{\rm so} A_T^{1/3} + r_{\rm so}^{(0)}, \tag{15}$$

with $a_{\rm so}$ being a constant.

The spin-orbit potential parameters in Eq. (14) and Eq. (15) were found to be not well defined by the experimental data used in the present analysis and were set to be zero in the global fitting procedure. They are discussed in Sec. V D.

4. Parametrization of GDP08

According to the previous considerations, the GDP08 global potential is parametrized by using 15 parameters in the following equations:

$$\begin{aligned} V_r &= V_0 + V_e(E - E_C), \quad E_C = \frac{6 Z_P Z_T e^2}{5 R_C}, \\ R_0 &= r_0 A_T^{1/3} + r_0^{(0)}, \quad a_0 = a_0, \\ W_v &= W_{\rm v0}\left[1+\exp\left(\frac{W_{\rm ve0}-(E-E_C)}{W_{\rm vew}}\right)\right]^{-1}, \\ W_s &= (W_{\rm s0} \pm W_{\rm st}\varepsilon) \times \left[1+\exp\left(\frac{(E-E_C)-W_{\rm se0}}{W_{\rm sew}}\right)\right]^{-1} \\ &\quad (+ \text{ for } ^3\text{He and } - \text{ for } ^3\text{H}), \\ \varepsilon &= (N_T - Z_T)/A_T, \quad R_{\rm wv} = R_{\rm ws} = r_w A_T^{1/3} + r_w^{(0)}, \\ a_{\rm wv} &= a_{\rm ws} = a_w, \quad R_C = 1.24 A_T^{1/3} + 0.12. \end{aligned} \tag{16}$$

III. EXPERIMENTAL DATABASE AND ANALYSIS PROCEDURES

A. Database for ^{3}He-nucleus elastic scattering

We have made an effort to collect nearly all the experimental angular distributions of differential cross sections of the ^{3}He-nucleus elastic scattering that could be found in the electronically available literature. All the data points were obtained by digitization of the figures or taken from tables in the individual papers except for the data of ^{3}He elastic scattering from ^{12}C, ^{58}Ni, and ^{90}Zr at 443 MeV [31], from ^{13}C at 450 MeV [32], from ^{14}N at 26.3 MeV, and from ^{20}Ne at 25.83 MeV. These data were taken from the EXFOR library [33]. In total, there are 515 sets of angular distributions, which are depicted in Fig. 4 as points in the $E_{\rm inc} - A_T$ distribution plot, where the filled points represent the data included in the present global analysis whose references are listed in Table I. Many of the data in the figures were in ratio-to-Rutherford units ($d\sigma/d\sigma_R$). For those cases they have been converted to absolute units by

$$\frac{d\sigma}{d\Omega}(\theta_i) = \left(\frac{d\sigma}{d\sigma_R}\right)_i \times \frac{d\sigma_R}{d\Omega}(\theta_i),$$

for each data point at center-of-mass angle θ_i, where the differential Rutherford cross section was calculated by

$$\frac{d\sigma_R}{d\Omega}(\theta_i) = 1.2959 \times \left(\frac{Z_P Z_T}{E_{\rm inc} \times A_T/(A_T + A_P)}\right)^2 \Big/ \sin^4(\theta_i/2), \tag{17}$$

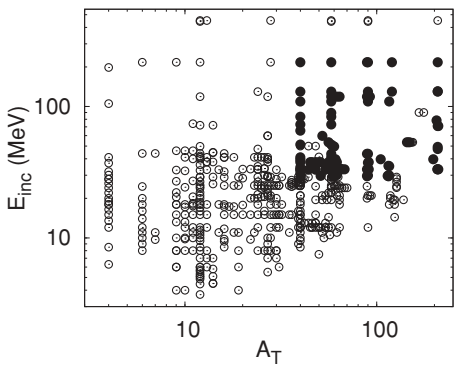

FIG. 4. Energy and target mass distributions of the angular distribution of differential cross sections collected for ^{3}He-nucleus scattering. The bigger filled points represent the data included in the present analysis.

TABLE I. Database of the ^{3}He-nucleus scattering included in the present analysis and their corresponding Q^2 values [see Eq. (18)] with the GDP08 global potential.

Target	E	Q^2	Ref.	Target	E	Q^2	Ref.	Target	E	Q^2	Ref.
^{40}Ca	31	131.9	[36]	^{58}Ni	109.2	29.7	[16]	^{89}Y	217	49.6	[40]
^{40}Ca	32.9	110.7	[41]	^{58}Ni	119	26.0	[17]	^{90}Zr	29.8	32.3	[45]
^{40}Ca	34.4	140.0	[36]	^{58}Ni	130	37.8	[51]	^{90}Zr	33.3	16.8	[46]
^{40}Ca	37.7	114.0	[34]	^{58}Ni	217	31.4	[40]	^{90}Zr	37.4	35.1	[44]
^{40}Ca	39.3	151.8	[36]	^{58}Fe	37.7	67.3	[44]	^{90}Zr	43.7	62.7	[34]
^{40}Ca	41	184.8	[39]	^{59}Co	29.5	33.0	[45]	^{90}Zr	109.2	20.0	[16]
^{40}Ca	51.4	98.1	[35]	^{59}Co	34.8	45.1	[45]	^{90}Zr	119	32.2	[17]
^{40}Ca	65.3	77.6	[37]	^{59}Co	37.7	87.2	[54]	^{90}Zr	130	36.2	[51]
^{40}Ca	73.2	121.5	[35]	^{59}Co	50	91.1	[55]	^{90}Zr	217	35.7	[40]
^{40}Ca	83.5	238.7	[35]	^{59}Co	119	33.7	[17]	^{91}Zr	33.3	12.8	[46]
^{40}Ca	109.2	25.1	[16]	^{60}Ni	29.5	67.9	[45]	^{91}Zr	37.7	17.1	[30]
^{40}Ca	130	89.5	[38]	^{60}Ni	33	20.8	[53]	^{92}Zr	119	54.7	[17]
^{40}Ca	217	24.2	[40]	^{60}Ni	33.7	42.7	[50]	^{105}Pd	39.7	10.2	[57]
^{44}Ca	33.1	51.1	[42]	^{60}Ni	35.1	71.3	[45]	^{114}Cd	29.7	7.6	[45]
^{45}Sc	37.7	108.6	[43]	^{60}Ni	49.7	68.0	[56]	^{115}In	29.8	14.8	[45]
^{46}Ti	37.7	76.5	[30]	^{60}Ni	50	61.2	[55]	^{115}In	35.3	7.5	[45]
^{48}Ca	33.1	89.0	[42]	^{60}Ni	119	24.2	[17]	^{116}Sn	29.8	31.5	[45]
^{48}Ti	37.7	93.5	[44]	^{61}Ni	39.7	62.2	[57]	^{116}Sn	35.2	16.7	[45]
^{50}Ti	37.7	85.4	[30]	^{62}Ni	30	32.5	[58]	^{116}Sn	109.2	59.1	[16]
^{54}Fe	29.6	68.4	[45]	^{62}Ni	33	18.6	[53]	^{120}Sn	130	17.2	[51]
^{54}Fe	37.7	65.8	[30]	^{62}Ni	33.7	37.1	[50]	^{120}Sn	217	78.5	[40]
^{54}Fe	33.3	43.0	[46]	^{62}Ni	37.7	26.2	[30]	^{144}Sm	53.4	54.0	[59]
^{56}Fe	33.5	65.9	[48]	^{62}Ni	119	32.9	[17]	^{148}Sm	53.4	32.3	[60]
^{56}Fe	37.7	36.5	[34]	^{63}Cu	33.3	18.5	[50]	^{197}Au	39.7	10.5	[57]
^{56}Fe	53.4	61.9	[47]	^{64}Ni	33	22.3	[53]	^{205}Tl	78.4	19.5	[61]
^{58}Ni	33	32.9	[53]	^{64}Ni	33.7	35.2	[50]	^{207}Pb	33.3	54.1	[46]
^{58}Ni	33.7	84.6	[50]	^{64}Ni	119	37.2	[17]	^{208}Pb	33.3	17.1	[46]
^{58}Ni	34.1	84.0	[52]	^{64}Zn	33.2	90.7	[50]	^{208}Pb	47.5	79.1	[63]
^{58}Ni	37.4	46.3	[44]	^{65}Cu	33.3	24.4	[50]	^{208}Pb	49.2	74.8	[62]
^{58}Ni	37.7	29.5	[34]	^{66}Zn	33.2	105.5	[50]	^{208}Pb	71.1	48.0	[64]
^{58}Ni	41	76.0	[39]	^{68}Zn	33.2	59.6	[50]	^{208}Pb	130	37.9	[51]
^{58}Ni	43.7	48.0	[34]	^{89}Y	29.6	21.7	[45]	^{208}Pb	130.5	45.0	[62]
^{58}Ni	51.3	67.1	[49]	^{89}Y	33.3	8.7	[46]	^{208}Pb	217	37.2	[40]
^{58}Ni	73.2	77.0	[35]	^{89}Y	43.7	37.6	[34]	^{209}Bi	33.3	56.7	[46]
^{58}Ni	83.5	81.3	[35]	^{89}Y	119	81.9	[17]	^{209}Bi	71.1	49.6	[64]
^{58}Ni	89.3	41.7	[16]								

with $A_{P,T}$ and $Z_{P,T}$ being the mass and atomic numbers of the projectile and the target, respectively.

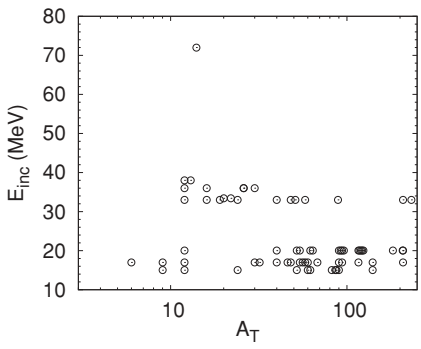

FIG. 5. Energy and target mass distributions of the angular distribution of differential cross sections collected for ^{3}H-nucleus scattering.

The radioactive nature of ^{3}H severely limits the number of ^{3}H-nucleus elastic scattering data, compared to those for ^{3}He. Only 68 sets of angular distributions were found in the literature; these are shown in Fig. 5 as points. Simultaneous fitting of both ^{3}He and ^{3}H scattering should better constrain the isospin asymmetry terms of the global potential. However, because the ^{3}H scattering database is relatively small and most of these data are at low energies where the energy dependence of the real potential is not clear at present (see Sec. V B), we did not include these data in the global analysis. We will show in Sec. IV F that the present GDP08 parameters account for these ^{3}H scattering data rather well.

B. Data included in the fitting procedure

The range of the present analysis (i.e., $40 \leqslant A_T \leqslant 209$ and $30 \leqslant E_{\rm inc} \leqslant 217$ MeV) was determined by the following considerations:

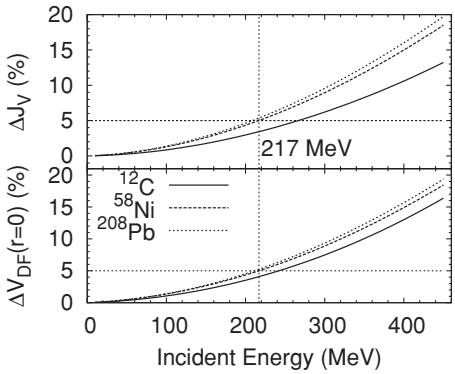

FIG. 6. Energy dependence of the relativistic effect of the DFP for ^{3}He from ^{12}C, ^{58}Ni, and ^{208}Pb targets. See the text for details.

(i) According to the double-folding calculations, as is shown in Fig. 1, the parametrization of the depth of the real potential, which is based on the assumption that V_r does not depend on the mass of the target, is only valid at large A_T values. For this reason only data corresponding to $A_T \geqslant 40$ were considered in this fitting procedure.

(ii) It was found that the real potential depth of the ^{3}He-nucleus optical potential deviates from the linear energy dependence at low energies starting from around 30 MeV for nuclei of mass $A_T \sim 58$ [18,39,65]. To avoid this complexity, in the present analysis we only include the elastic scattering data with $E_{\rm inc} \geqslant 30$ MeV.

(iii) When the incident energy of ^{3}He is high enough, relativistic effects, at least the relativistic kinematics, have to be taken into account. Again we use double-folding model calculations for our guidance. Figure 6 shows the differences of $V_{\rm DF}^{(0)}$ and J_V of the DFP for ^{3}He on ^{12}C, ^{58}Ni, and ^{208}Ni targets at incident energies from 10 to 450 MeV, that is,

$$\Delta V_{\rm DF}^{(0)} = 100 \times \left[V_{\rm DF_{rel}}^{(0)} - V_{\rm DF_{nonrel}}^{(0)}\right] / V_{\rm DF_{rel}}^{(0)},$$
$$\Delta J_V = 100 \times (J_{V_{\rm rel}} - J_{V_{\rm nonrel}}) / J_{V_{\rm rel}},$$

where the quantities calculated with and without taking into account relativistic kinematics are discriminated by "rel" and "nonrel" in their subscripts, respectively. One can see that for most of the experimental data in the present analysis the relativistic effect is smaller than 5%, except for the data at 217 MeV, for which the relativistic effect is around 5.2% for the heavy targets. We thus do not include the 443- and 450-MeV data to avoid the explicit treatment of the relativistic effects.

The optical model program OPTICS used in MINOPT is nonrelativistic. The relativistic effects were not taken into account in the present work for the following reasons [8]: (i) As has been shown by double-folding calculations, the relativistic effect for the data under consideration is small, and (ii) part of our goal is to provide, for this energy range, a potential useful in nuclear physics calculations, which are usually made with Schrödinger equations. However, we will show that when taking into account the relativistic kinematics the GDP08 global potential can reproduce the experimental data at 443 and 450 MeV rather well.

Within this range the ^{40}Ca, ^{44}Ca, and ^{48}Ca data at 50.4 MeV [66] and ^{52}Cr data at 59.8 MeV [56] were not included because they were found to always give much larger Q^2 values compared to the Q^2 values of these targets at other energies and of the other targets at nearby energies. The ^{150}Sm, ^{152}Sm, and ^{154}Sm data at 53.4 MeV [60] and the ^{166}Er and ^{176}Yb data at 90.0 MeV [67] were not included because these nuclei have large deformations and the optical model used in OPTICS may not be suitable for them.

We included all data points at all angles for all the experimental data except for data points of (i) the ^{40}Ca data at 31.0, 32.9, 34.4, 39.3, 41.0, and 83.5 MeV with center-of-mass angles ($\theta_{\rm c.m.}$) larger than 100°, (ii) the ^{66}Zn data at 33.2 MeV with $\theta_{\rm c.m.}$ larger than 142°, and (iii) the ^{148}Sm data at 53.4 MeV with $\theta_{\rm c.m.}$ larger than 106°. The criterion of removing those data points was merely the corresponding Q^2 values of these data sets. One can see from Table I that even when removing data points at larger angles the Q^2 values of data sets in cases (i) and (ii) are still among the largest in the whole database. The reason for case (iii) is that the error bars for the removed data points are much larger than the data points at smaller angles and inclusion of those data points also results in values of Q^2 that are too high.

Note that although isospin asymmetry dependence has been introduced in the parametrization of the GDP08 potential (Sec. II C4), users of this global potential should always be cautious when applying it to nuclei that are far away from the stability line because almost all data included in the present analysis are for nuclei that are near the valley of stability.

C. Uncertainties of the experimental data

Besides the normal statistical and systematic uncertainties, the experimental data have additional uncertainties introduced by the digitization process we used. By checking some of the data carefully and sometimes repeating the digitization several times we estimate the digitization errors to be less than 0.5° in determining the angles and less than 5% in determining the differential cross sections. For illustration, we use the data for ^{51}V(^{3}He,^{3}He)^{51}V scattering at 29.6 MeV [45]. In Ref. [45] the authors presented the differential cross sections both in tables in absolute units and figures in ratio-to-Rutherford units. The comparison between the tabulated and digitized data are shown in Fig. 7. In this case, the standard deviations of the uncertainties of the scattering angles and differential cross sections are 0.476° and 2.29%, respectively. Of course, the digitization errors also depend on the quality of the figures.

Different data sets measured by different groups with different facilities may have different systematic uncertainties. This can be approximately corrected by the Q^2 renormalization method described in Ref. [8]. In most of the papers only the statistical uncertainties were reported. However, the elastic scattering measurements were usually made with high statistical precision, which makes the statistical uncertainties unimportant except for some data at backward angles. Because of these considerations, we assume a uniform uncertainty of 5% for all the data sets in the fittings.

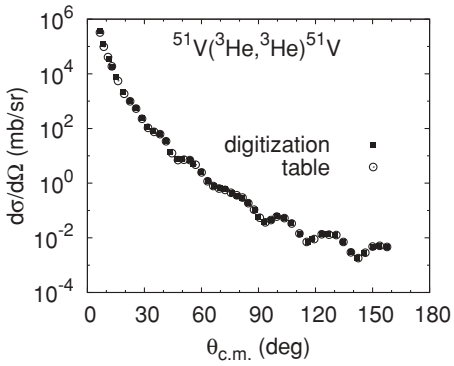

FIG. 7. Comparison of tabulated data (open points) and digitized data (closed points) of the angular distributions of ^{3}He elastic scattering from ^{51}V at 29.6 MeV [45]. The digitized data were converted from $d\sigma/d\sigma_R$ to absolute units.

D. Fitting procedures

The experimental data were simultaneously fitted by using the computer program MINOPT by minimizing the following quantity:

$$Q^2 = \frac{1}{N}\sum_{i=1}^{N}\frac{1}{M_i}\sum_{j=1}^{M_i}\frac{\left[\sigma_{ij}^{\exp}-\sigma_{ij}^{\mathrm{th}}(\vec{p})\right]^2}{\Delta\sigma_{ij}^2}, \tag{18}$$

where N is the number of angular distribution sets, M_i is the number of data points of the ith angular distribution, and $\sigma_{ij}^{\exp}$ and $\sigma_{ij}^{\mathrm{th}}$ are the values of differential cross sections of the jth point in the ith set of data (with experimental error of $\Delta\sigma_{ij}$) and its corresponding theoretical value calculated using the vector of parameters $\vec{p}$. The quantity Q^2 is usually referred to as χ^2. However, as has been pointed out in Ref. [8], Q^2 has a χ^2 distribution only when each term of Q^2 is normally distributed with a standard deviation of one and a mean of zero. In the search of global potential parameters, where a certain amount of experimental data with different systematic uncertainties are fitted simultaneously, the quantity Q^2 does not have these desirable properties, so we named it differently. For the entire database, $N = 106$, but Q^2 can be applied to individual data sets as well, using $N = 1$.

We started the fitting procedures by using the parameters of the CH89 nucleon-nucleus potential as the initial values with the depth parameters V_0, W_{v0}, and W_{s0} multiplied by 3 and V_{so} taken to be 2.0 MeV fm^2, including all the parameters in the parametrization of CH89. Then we did numerous test fittings using different initial values. This procedure eventually helped us to find the most likely region of the optimum potential parameters. Also in this process we found that the spin-orbit potential and the isospin asymmetry term of the real potential, which exist in the CH89 parametrization, are not well determined by the experimental data included in the present analysis. For this reason we did not include these parameters in the final parametrization of GDP08.

Once we found the *nearly optimal* global potential, we performed a large number of test fittings with the initial values of the parameters randomly chosen in this region. This process eventually provided us with several candidates for the best set of parameters, with each of these parameter sets satisfying the convergence criteria of the MIGRAD strategy of MINUIT [20].

One of the unique features of the MINOPT program is that it can estimate the uncertainty of the parameters and the parameter correlations [8]. The candidates for the best global potentials were then tested by performing searches using the best global values randomly changed by 10% as initial parameter values. The results were then checked to see whether the parameter values were consistent, within the estimated uncertainties, with the best values. In this way we determined the best global potential, which is reported in the next section.

IV. RESULTS

A. Parameters of GDP08

The final GDP08 parameters and uncertainties are listed in Table II. The uncertainties are standard deviations of the bootstrap distributions for each parameter, as are shown in Fig. 8.

B. Uncertainties and correlation coefficients between the global parameters

There are at least three facts that make the study of the uncertainties and correlations between the parameters important: (i) The potential parameters are derived from experimental data with uncertainties, (ii) the optical model we are using is not a complete description of the scattering for every target at all energies, and (iii) there are known correlations between the parameters, for example, the $V_r R^n \approx$ constant relation between the real potential parameters [68], that make a high-precision determination of the optical potential parameters impossible by only using elastic scattering data.

The definition of parameter uncertainty and correlation coefficients can be found in Ref. [8]. For convenience, we give a brief summary of the discussion here. A common measure

TABLE II. Parameters of the GDP08 global optical potential for the $A = 3$ nuclei.

Parameter	Value	Uncertainty	Units
V_0	118.3	1.3	MeV
V_e	−0.13	0.01	
r_0	1.30	0.01	fm
$r_0^{(0)}$	−0.48	0.05	fm
a_0	0.82	0.01	fm
W_{v0}	38.5	3.9	MeV
W_{ve0}	156.1	11.9	MeV
W_{vew}	52.4	8.2	MeV
W_{s0}	35.0	1.1	MeV
W_{st}	34.2	8.0	MeV
r_w	1.31	0.02	fm
$r_w^{(0)}$	−0.13	0.10	fm
a_w	0.84	0.01	fm
W_{se0}	30.8	4.7	MeV
W_{sew}	106.4	8.0	MeV
r_c	1.24	fixed	fm
$r_c^{(0)}$	0.12	fixed	fm

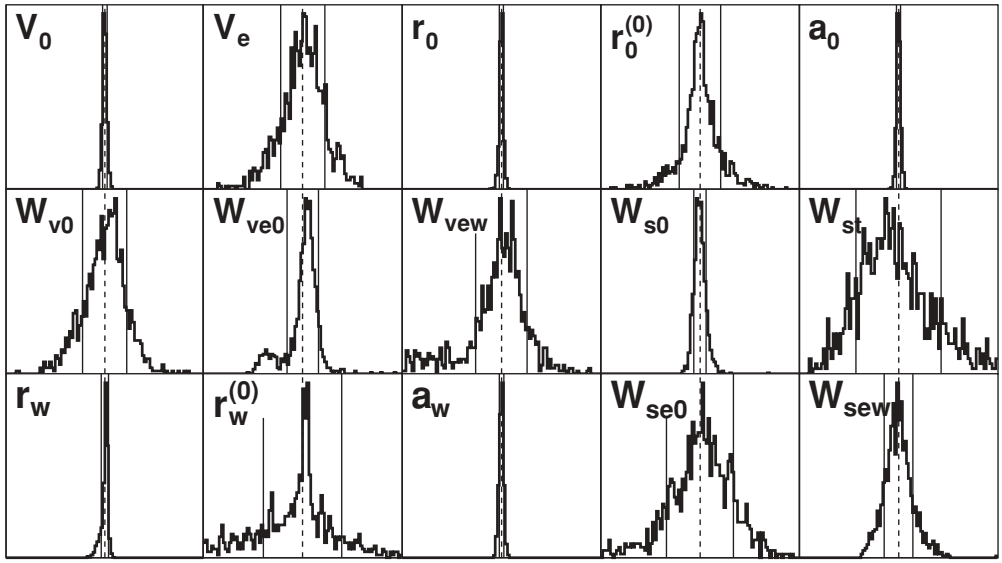

FIG. 8. Bootstrap distributions of the GDP08 optical model parameters. The horizontal axes show $x = p/\overline{p} - 1$, where $\overline{p}$ is the mean value of the parameter in the bootstrap distribution. They are scaled to show x values within the interval $[-0.5, 0.5]$. The point $x = 0$ is shown by the dashed line. The solid lines show the standard error interval. The bootstrap was performed with 1000 samples of the 106 angular distribution database.

of the uncertainty of a quantity x is the *standard deviation*,

$$\sigma = \left(\frac{1}{N} \sum_i (x_i - \overline{x})^2 \right)^{1/2}, \tag{19}$$

where $\overline{x}$ estimates the mean value of x from N repeated measurements. If the distribution of x_i over $i = 1, 2, \ldots, N$ is normal (Gaussian) the standard deviation is the half-width of an interval that contains 68% of all the observations [i.e., the probability $P(\overline{x} - \sigma < x < \overline{x} + \sigma) = 0.68$].

If two or more quantities are measured simultaneously, both the uncertainty in each and the degree to which variations in one parameter, x, can affect determination of another, y, should be described. The relation between x and y is usually described by the *correlation coefficient*,

$$\rho(x, y) = \frac{\sum_i (x_i - \overline{x})(y_i - \overline{y})}{\left[\sum_i (x_i - \overline{x})^2 \sum_i (y_i - \overline{y})^2\right]^{1/2}}, \quad -1 \leqslant \rho \leqslant 1, \tag{20}$$

in which the sum is over N repeated measurement pairs (x_i, y_i). Here $\rho = +1$ indicates perfect correlation of x and y in the same direction, and $\rho = -1$ means they are perfectly anticorrelated. Correlation coefficients are useful in two ways: (i) as a measure of the interdependence of two variables and (ii) in the propagation of uncertainty for functions depending on both x and y.

In MINOPT the uncertainties and correlations coefficients of the global potential parameters can be calculated by using the bootstrap uncertainty analysis method [69–71]. The correlations show whether the global optical model parameters in GDP08 are strongly interdependent and allow estimates of the uncertainties for functions of the parameters such as the volume integrals J_V and J_W. The importance and the application of the uncertainties and correlation coefficients were discussed thoroughly in Ref. [8]. Here we only give the results for the GDP08 potential, listed in Tables II and III and visualized in Figs. 8 and 9. Note that in the global analysis of GDP08 the well-known strong anticorrelations between the central-well depth V_0 and its radius $R_0 = r_0 A_T^{1/3} + r_0^{(0)}$ for single angular distributions is weakened [$\rho(V_0, r_0) = -0.3$, $\rho(V_0, r_0^{(0)}) = -0.1$], presumably because of the large variation of nuclear radii over $40 \leqslant A_T \leqslant 209$. Thus the well depth V_0 and the radii r_0 and $r_0^{(0)}$ are determined independently and without ambiguity. This was also found in the CH89 global nucleon-nucleus potential [8].

Similar to those found in the CH89 global nucleon-nucleus potential [8], the least well determined parameters in the GDP08 potential are those for (i) the energy dependence of the absorptive potential ($W_{\rm ve0}$, $W_{\rm vew}$, $W_{\rm se0}$, and $W_{\rm sew}$), (ii) the offsets of the radius parameters ($r_0^{(0)}$ and $r_w^{(0)}$), and (iii) the isovector components of the absorptive potential ($W_{\rm st}$). The case (i) is partially a consequence of the irregular distribution of the data in energy. Comparison of the energy dependence of the absorptive potential (see Fig. 10) with the distribution of the data (see Fig. 4) shows that the variation of W_s and W_v with energy is greatest where there is the least amount of data, around 130 to 200 MeV. Case (ii) is because $r_0^{(0)}$ and $r_w^{(0)}$ are highly correlated with r_0 and r_w, respectively, as is shown in Table III and Fig. 9. Finally, although $W_{\rm st}$ is poorly determined, its uncertainty is consistent with those in the other depth parameters.

C. GDP08 prediction of elastic scattering data

In this section we compare the experimental data with the results of optical model calculations using the GDP08 global potential. The calculations were made using FRESCO [72] as a cross-check of the optical model code OPTICS incorporated in MINOPT. We compare the calculations with experimental

TABLE III. Correlation coefficient estimated for best-fit parameter values in GDP08. For corresponding parameters and uncertainties, see Table II. All correlation coefficients of absolute value less than 0.1 have been omitted. The uncertainty of any single element is ±0.1.

	V_0	V_e	r_0	$r_0^{(0)}$	a_0	W_{v0}	W_{ve0}	W_{vew}	W_{s0}	W_{st}	W_{se0}	W_{sew}	r_w	$r_w^{(0)}$
V_e	−0.3													
r_0	−0.3	−0.4												
$r_0^{(0)}$	−0.1	0.4	−0.9											
a_0	0.5	0.4	−0.6	0.3										
W_{v0}	−0.3	0.5	−0.1	0.1	0.2									
W_{ve0}	−0.2	−0.2	0.2	−0.1	−0.2	0.5								
W_{vew}	–	−0.3	0.1	−0.2	–	0.4	0.8							
W_{s0}	−0.1	0.1	–	0.1	−0.2	−0.1	−0.3	−0.6						
W_{st}	0.2	–	0.1	−0.2	–	−0.2	−0.2	−0.3	–					
W_{se0}	−0.1	−0.2	0.2	−0.1	−0.4	–	0.2	−0.1	−0.1	−0.3				
W_{sew}	−0.1	−0.4	0.2	−0.1	−0.5	−0.3	0.4	0.3	−0.1	0.2	0.1			
r_w	–	−0.2	0.1	−0.1	0.1	0.2	0.3	0.5	−0.2	−0.7	0.2	−0.2		
$r_w^{(0)}$	0.1	0.4	−0.3	0.2	0.2	−0.1	−0.3	−0.3	0.1	0.6	−0.4	–	−0.9	
a_w	−0.1	−0.5	0.1	–	−0.4	−0.3	–	−0.1	–	–	0.1	0.4	–	−0.3

data corresponding to targets with mass A_T from 6 to 208 and covering a broad range of incident energy to test the reliability and the prediction power of the GDP08 global potential. The results are shown in Figs. 11–14.

Whenever possible, we compare with one of the most frequently used global potentials for ^{3}He published by Becchetti and Greenlees (BG) [14], which was obtained by systematic study in the region of $A_T > 40$ and $E_{\rm inc} < 40$ MeV, namely,

$$\begin{aligned} &V_r = 151.9 - 0.17E + 50(N_T - Z_T)/A_T, \quad r_0 = 1.20, \\ &a_0 = 0.72, \quad W_v = 41.7 - 0.33E + 44(N_T - Z_T)/A_T, \\ &r_w = 1.40, \quad a_w = 0.88, \quad V_{\rm so} = 2.5, \\ &r_{\rm so} = 1.20, \quad a_{\rm so} = 0.72, \quad r_c = 1.30. \end{aligned} \tag{21}$$

The units of the BG parameters are the same as those of GDP08. One can see that at low energies GDP08 and BG potentials give similar results to the elastic scattering data; however, the BG potential will not be able to reasonably reproduce the experimental data when the incident energy of the ^{3}He projectile is higher than about 40 MeV whereas GDP08 behaves very well at high energies for all the targets from $A = 6$ to $A = 208$.

D. Total reaction cross sections

The total reaction cross section of ^{3}He on targets from ^{9}Be to ^{208}Pb at 96.4, 137.8, and 167.3 MeV measured by Ingemarsson *et al.* [94] are compared to the optical model

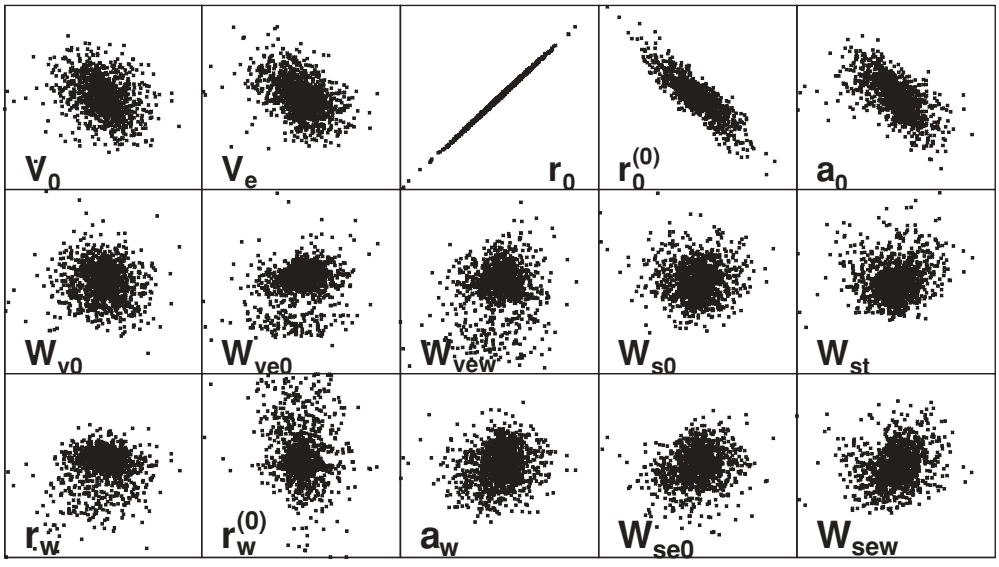

FIG. 9. Scatter plots of correlated parameters. The figure shows the correlation of r_0 with all the other parameters in a bootstrap data set of 1000 samplings of the global database. The axes are scaled so that the correlation ellipses would be aligned along a 45° line if the relative uncertainties in each pair of parameters were correctly estimated, as shown for the self-correlation of r_0.

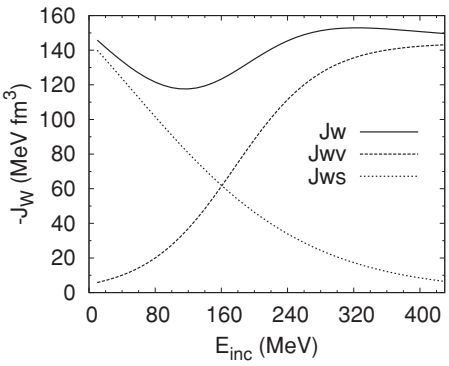

FIG. 10. Energy dependence of the absorptive potentials for GDP08. The volume integrals of the surface (J_{WS}) and volume (J_{WV}) absorption are shown by dotted and dashed curves, respectively, and the total absorptive volume integral ($J_W = J_{WS} + J_{WV}$) is shown by the solid line. The calculations are made for ^{3}He scattering from ^{58}Ni. Coulomb corrections and the isospin asymmetry term for the surface absorption (W_{st}) are included in the calculations.

predictions using the GDP08 global potential in Fig. 15. One can see that GDP08 reproduces the total reaction cross section data rather well for targets with $A_T > 100$ and overestimates the experimental data as A_T decreases. From the figures we have shown in Sec. IV C one can expect that the GDP08 should be able to reproduce the elastic scattering data at these three energies satisfactorily. The discrepancy between the theoretical predictions and the experimental data here might be because the elastic scattering and total reaction data have different sensitivities to different sets of S-matrix elements [95].

E. Upper limit of the incident energy for the application of GDP08

We verify here that, when taking into account relativistic kinematics, the GDP08 parameters can be used for ^{3}He elastic scattering at energies where the relativistic effects are important. Figure 16 shows the comparison between the calculations using the GDP08 potential and the elastic scattering data of ^{3}He from ^{12}C, ^{58}Ni, and ^{90}Zr at 443 MeV [31], from ^{13}C at 450 MeV [32], and from ^{12}C, ^{28}Si, ^{58}Ni, ^{90}Zr, and ^{208}Pb at 450 MeV [96]. The calculations were made using the computer code ECIS03 [97] with and without taking into account relativistic kinematics, which are shown by solid and dashed curves, respectively. One can see that (i) relativistic effects are more important for heavy targets than for light targets and (ii) when relativistic kinematics were taken into account in the calculations, the phases of the angular distributions for targets of $A \geqslant 58$ are greatly improved when compared to the experimental data. The fact that, for the ^{58}Ni and ^{90}Zr targets at 443 MeV, both phases and absolute amplitudes of the differential cross sections are well reproduced whereas for the same targets at close energy of 450 MeV only the phases are well reproduced may suggest that there might be some normalization problem in the data sets at 450 MeV. Note that the absolute cross sections in Refs. [31,32] were converted to ratio-to-Rutherford units in Fig. 16 with relativistic kinematics explicitly taken into account for their corresponding Rutherford cross sections.

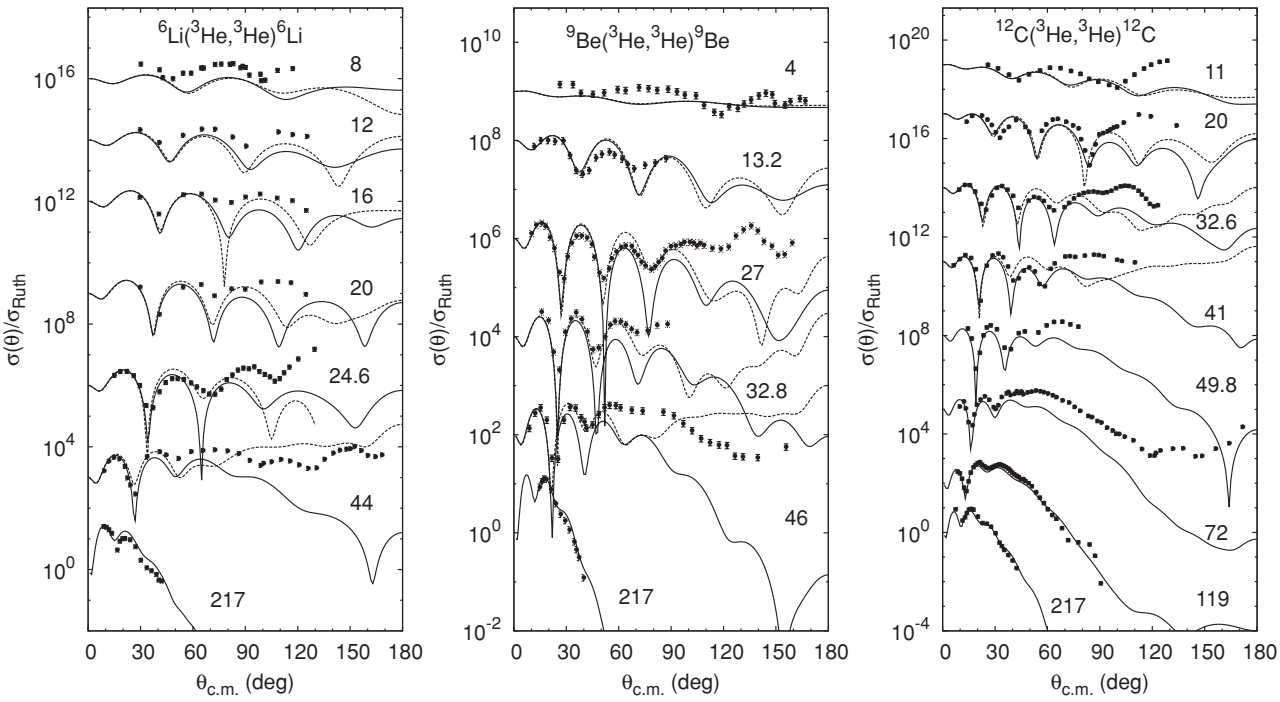

FIG. 11. Comparison between the optical model calculations and experimental data of ^{3}He elastic scattering from ^{6}Li, ^{9}Be, and ^{12}C at different energies [17,39,40,73–82]. The solid and dashed curves were calculated by using the GDP08 and BG global potentials, respectively. All data are shown as points with the same style. Different data sets are offset by factors of 10^n with n variable for optimum view.

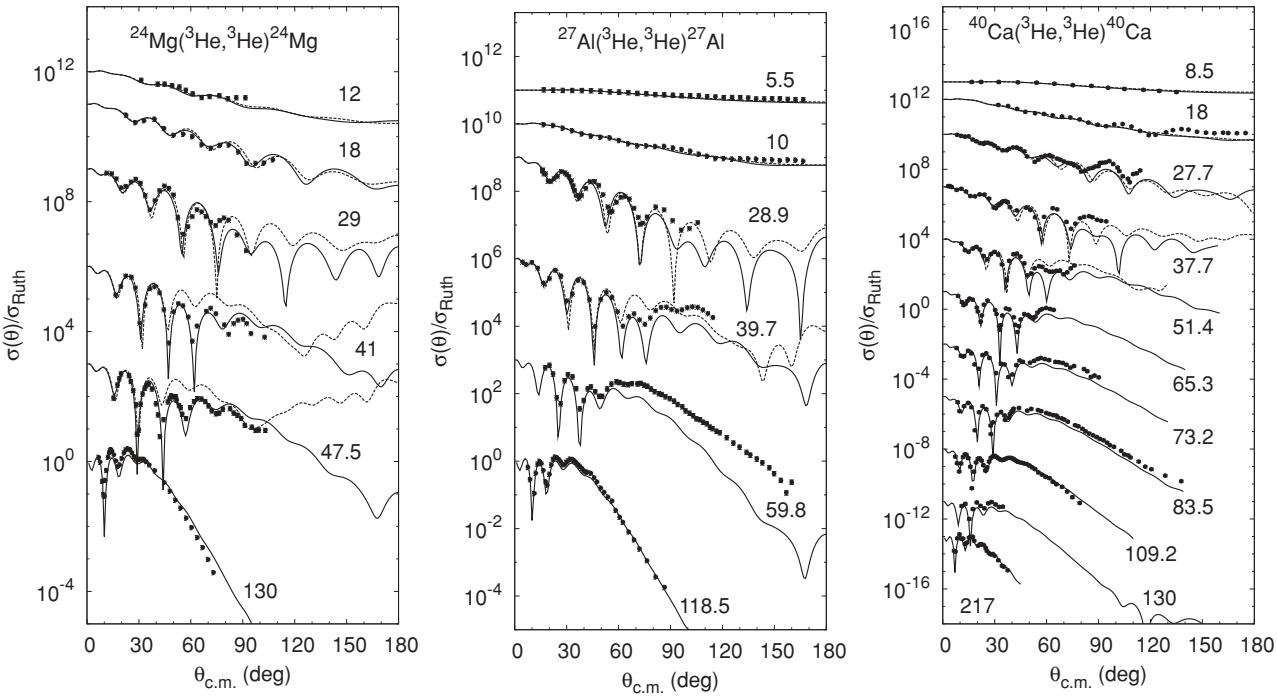

FIG. 12. Same as Fig. 11, but with ^{24}Mg, ^{27}Al, and ^{40}Ca targets [16,17,34,35,37–40,51,56,57,83–90].

F. GDP08 application to triton elastic scattering

Recently, Li *et al*. studied the global triton optical potential [15] using 29 parameters to fit 36 sets of ^{3}H-nucleus scattering data within the range $46 \leqslant A_T \leqslant 232$ and $2.0 \leqslant E_{\rm inc} \leqslant 33$ MeV. Their resulting global potential for the triton is referred to as the Li potential in the following text. We compare calculations using GDP08 and the Li potential with the experimental data. The results are shown in Figs. 17–19. Again, the comparison over a large range of A_T and $E_{\rm inc}$ coverages allows one to estimate the performance of the global potential.

(i) For the 15-MeV data, GDP08 produces large oscillations in the angular distributions that are not consistent with

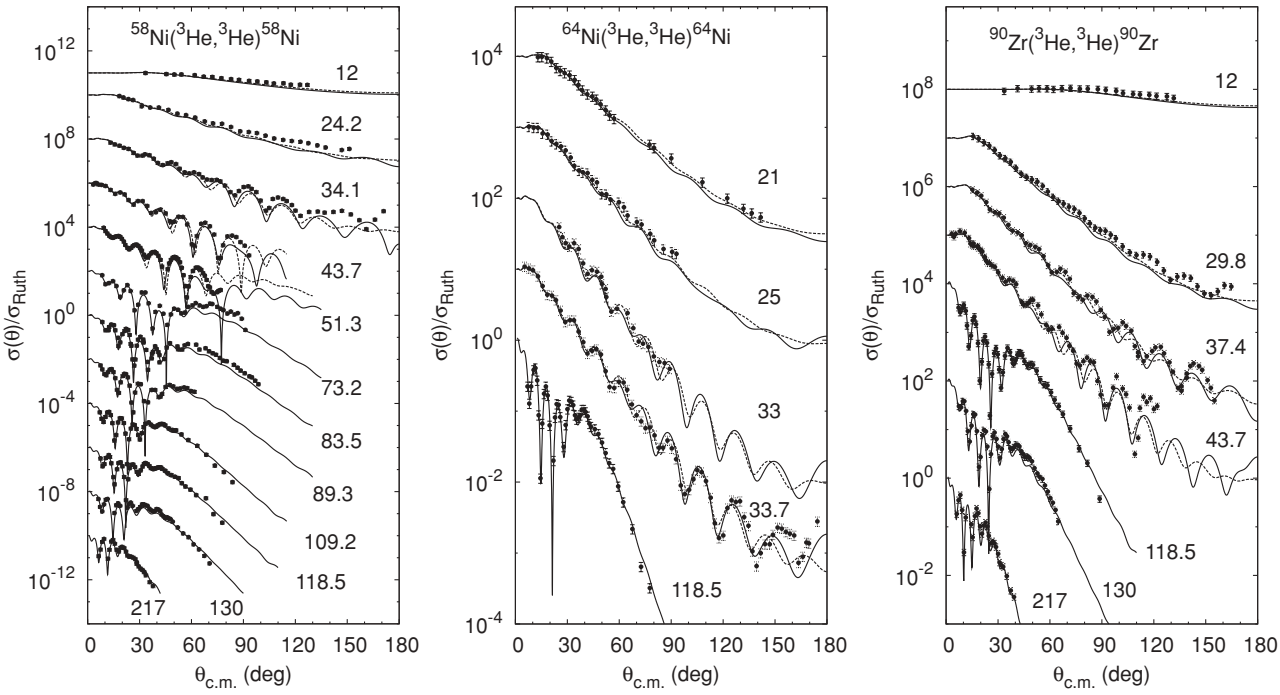

FIG. 13. Same as Fig. 11, but with ^{58}Ni, ^{64}Ni, and ^{90}Zr targets [16,17,34,35,40,44,45,49–53,83,91,92].

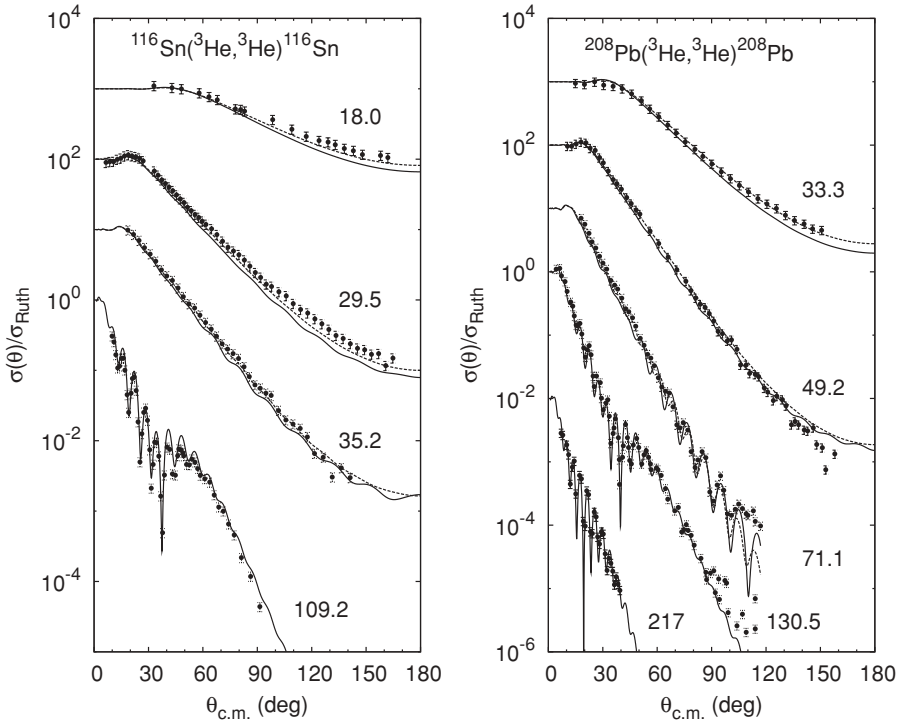

FIG. 14. Same as Fig. 11, but with ^{116}Sn and ^{208}Pb targets [16,40,45,46,62,64,93].

the experimental data compared to the Li potential, especially for targets of $A_T \leqslant 60$.

(ii) For the 17- and 20-MeV data, in general GDP08 is better than the Li potential in the sense that it reproduces better phases of the angular distributions of the differential cross sections. We found that the agreement with the $E_{\rm inc} \leqslant 20$ MeV and $50 \lesssim A_T \lesssim 120$ region could be greatly improved by reducing the depth parameter of the real potential of GDP08. We discuss this problem in Sec. V B.

(iii) GDP08 and the Li potential give similar results when compared with the $E_{\rm inc} = 33$ MeV data; however, at the higher energies of 36 and 38 MeV, GDP08 begins to be better than the Li potential. We recall that the surface

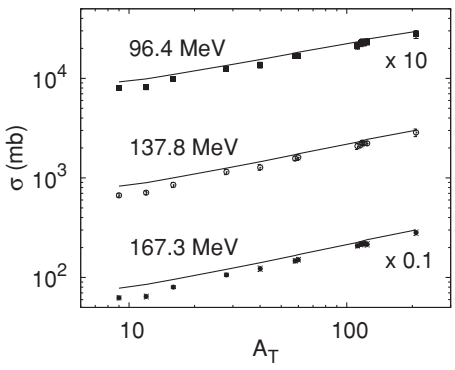

FIG. 15. Comparison between optical model calculations using the GDP08 global potential and measurements of the ^{3}He-nucleus total reaction cross sections [94] at 96.4, 137.8, and 167.3 MeV. The experimental data are shown in points with different symbols and model calculation results are represented by solid curves.

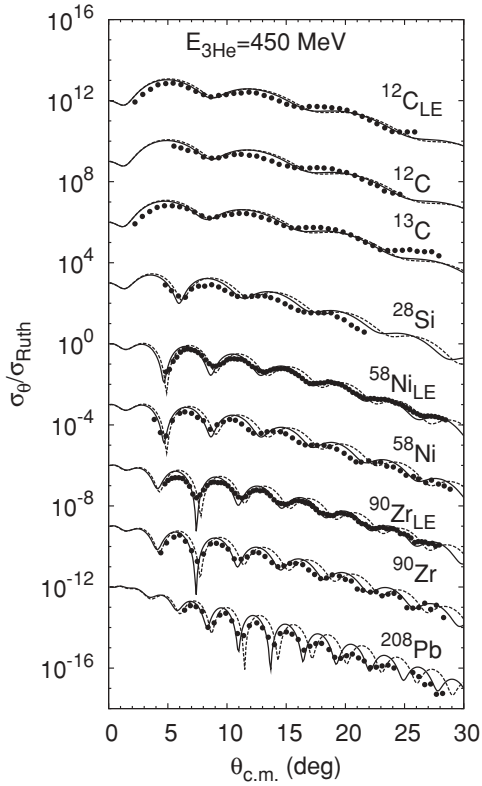

FIG. 16. Comparison between the optical model calculations using the GDP08 global potential and the measurements of the ^{3}He elastic scattering from different targets at 443 MeV (with subscripts "LE") and 450 MeV [31,32,96]. The solid and dashed curves were calculated using ECIS03 with and without taking into account relativistic kinematics, respectively. The differential cross sections were offset by factors of 1000.

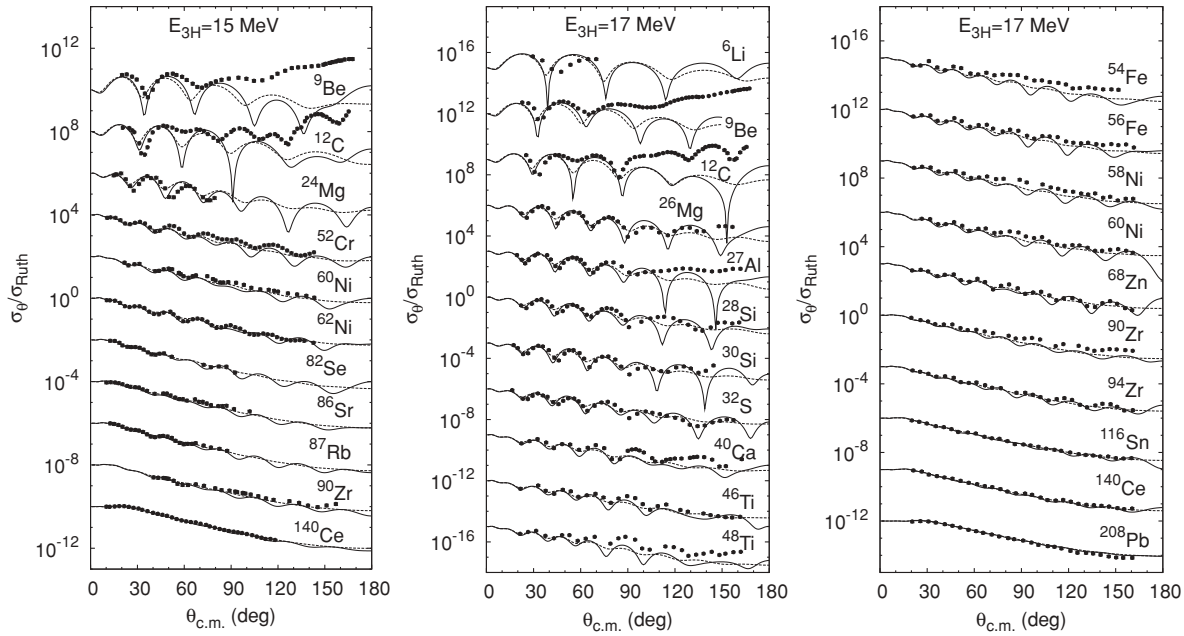

FIG. 17. Comparison between the optical model calculations and the experimental data of ^{3}H elastic scattering from different targets at $E_{\rm inc} = 15$ and 17 MeV [98–110]. The solid and dashed curves are results calculated using GDP08 and the Li potential, respectively. All data are shown as points with the same style. Different data sets are offset by factors of 10^n with n variable for optimum view.

imaginary part of the Li potential,

$$W_s = 37.06 - 0.6451E_{\rm inc} - 47.19(N_T - Z_T)/A_T,$$

makes the Li potential not applicable as soon as $E_{\rm inc}$ is larger than 57 MeV. In practice, by comparing to the ^{3}He-nucleus scattering data, we found that the Li potential could not give reasonable predictions to the experimental data for energies larger than around 40 MeV. We show in Fig. 20 that GDP08 works well at higher incident energies. The data are from ^{14}C elastic scattering from the ^{3}H target at 334.4 MeV, which corresponds to the incident energy of ^{3}H being 71.7 MeV for the ^{14}C target [112]. The shape of the experimental angular distribution could be well reproduced by the GDP08 potential, but the differential cross sections should be normalized by a factor of around 1.4 to get an acceptable reproduction of the absolute cross sections. This may not mean that GDP08 does not work well for this case because the authors declared in their text that "The obtained results are preliminary, because the absolute cross section will be measured with higher accuracy" [112].

Note that some data, for example, the ^{68}Zn data at 17 MeV, which were shown to be reproduced rather well with the Li potential using the computer code APMN [119] in Ref. [15], were not reproduced as well by using the same potential with the computer code FRESCO. This may be because APMN takes into account both compound nucleus elastic scattering and shape elastic scattering whereas the results shown in this work were calculated with only shape elastic scattering.

V. DISCUSSION

A. The doubly-magic nucleus ^{40}Ca

Among all the data included in the present analysis, the ^{40}Ca data at energies between 31.0 and 83.5 MeV are always those with the worst fit (see Fig. 12). We then did *regional* fittings with ^{40}Ca data only, keeping the same parametrization as in the global fitting except that in this case the $W_{\rm st}$ parameter is irrelevant and was set to be zero. The resulting parameters are listed in Table IV and the fits to the ^{40}Ca data using these parameters are shown in Fig. 21. One can see that the angular

TABLE IV. Optical potential parameters of the ^{3}He-^{40}Ca system from regional fitting.

Parameter	Value	Uncertainty	Units
V_0	124.3	5.4	MeV
V_e	−0.17	0.05	
r_0	1.27	0.02	fm
$r_0^{(0)}$	−0.32	0.06	fm
a_0	0.82	0.02	fm
$W_{\rm v0}$	13.1	6.4	MeV
$W_{\rm ve0}$	68.4	9.0	MeV
$W_{\rm vew}$	21.3	4.8	MeV
$W_{\rm s0}$	27.1	1.2	MeV
r_w	1.27	0.02	fm
$r_w^{(0)}$	0.40	0.05	fm
a_w	0.77	0.02	fm
$W_{\rm se0}$	52.0	11.2	MeV
$W_{\rm sew}$	169.7	47.4	MeV
r_c	1.24	fixed	fm
$r_c^{(0)}$	0.12	fixed	fm

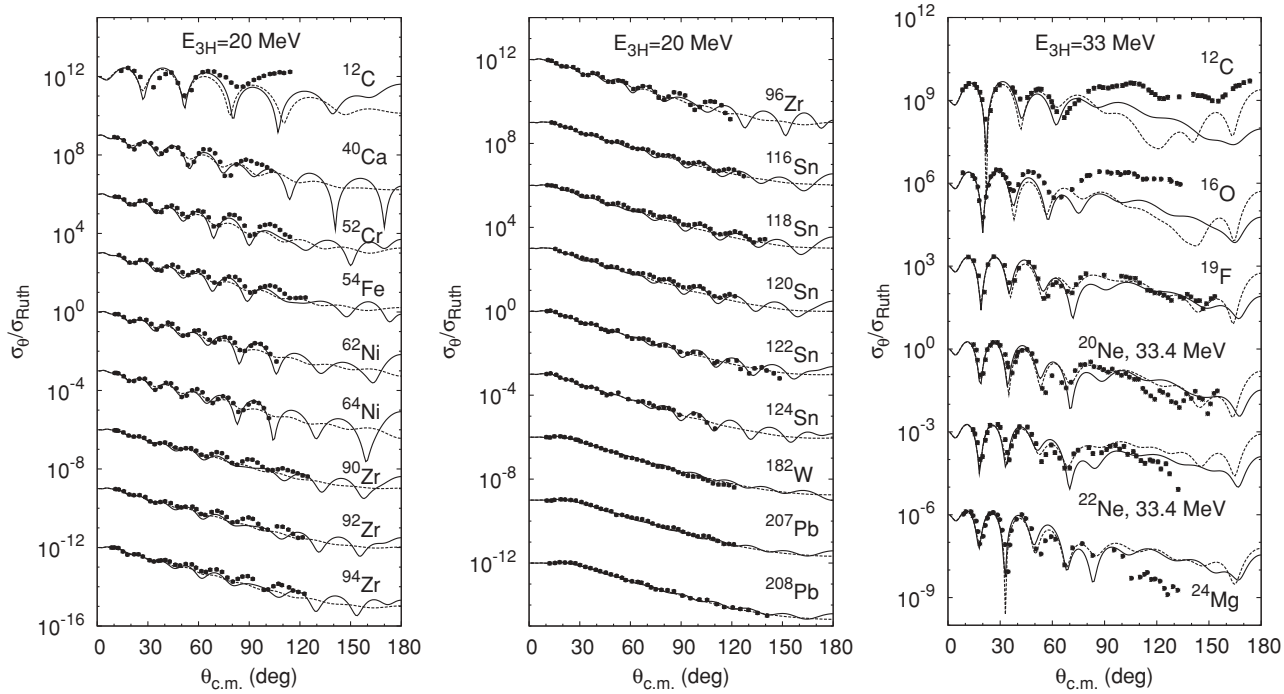

FIG. 18. Same as Fig. 17, but with $E_{\rm inc} = 20$ and 33 MeV [100,111,113–116].

distributions at energies between 31.0 and 83.5 MeV have been greatly improved. Note that the optical potential parameters obtained in this regional fitting are highly constrained by the larger number of low-energy data (with incident energies of 9 out of 13 sets of data being below 80 MeV). This leads to the unexpected poor fits to the 109.2- and 130-MeV data.

As pointed out by Trost *et al*. [18], a doubly-magic nucleus like ^{16}O or ^{40}Ca has a larger gap between its ground and first excited states as compared to other stable nuclei with $A_T > 10$, leading to reduced couplings between the elastic and nonelastic scattering channels, and thus requiring smaller absorption strength. This can be seen in Fig. 22, in which

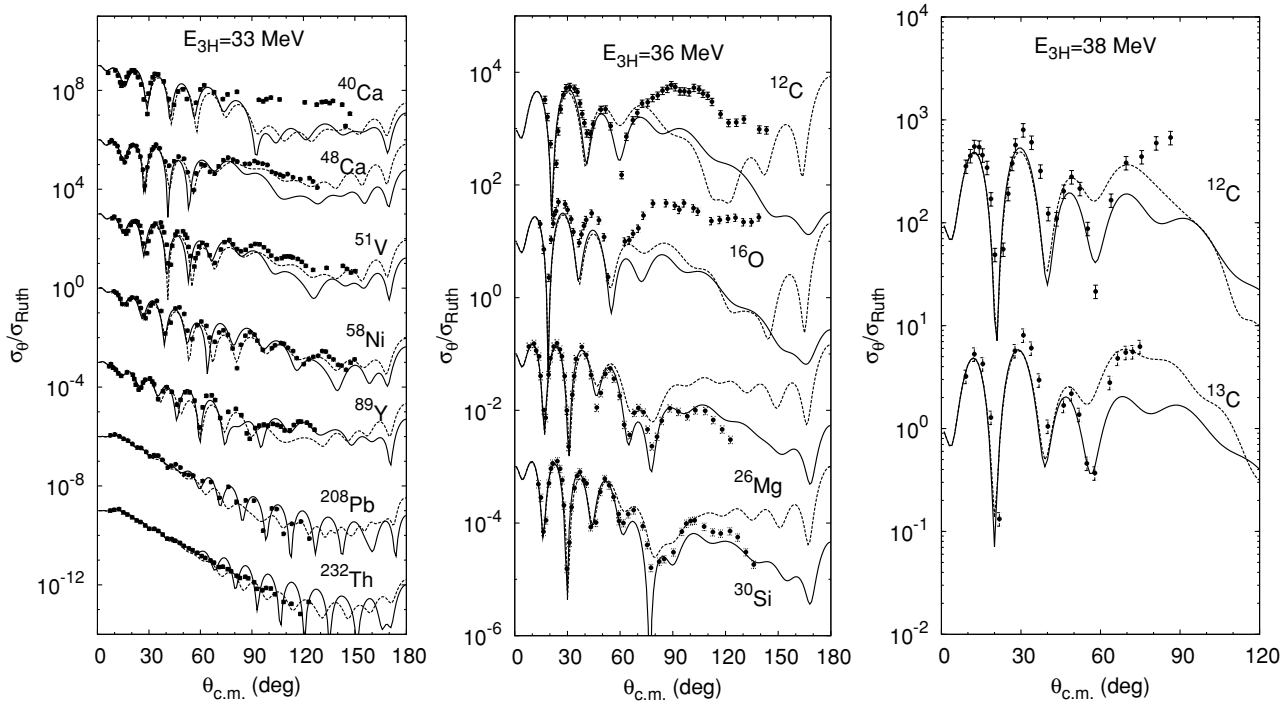

FIG. 19. Same as Fig. 17, but with $E_{\rm inc} = 33$, 36, and 38 MeV [115,117,118].

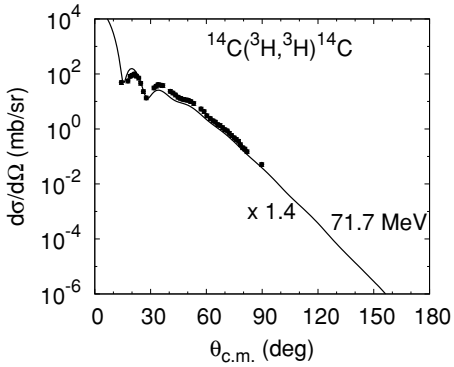

FIG. 20. Comparison between the optical model calculation using GDP08 and experimental data for ^{14}C elastic scattering from ^{3}H at 334.4 MeV (with ^{3}H energy being 71.7 MeV in *normal* reaction kinematics). The data were taken from Ref. [112].

the upper panel compares the imaginary part of the ^{3}He-^{40}Ca potential as a function of incident energy calculated using the *global* parameters in Table II (labeled with "glb") and the *regionally* fitted parameters in Table IV (labeled with "rgl"). The lower panel compares the corresponding $Q^2_{\rm rgl}/Q^2_{\rm glb}$ values for each data set. It is clear that the best fit of the data always requires the smaller J_W value whether it is in the global fitting or in the regional fitting. Here might be a good place to point out that the global potential, which does not take the different structure of every particular nucleus into account and is parametrized using smooth forms of energy and mass dependence, is thus only supposed to give *reasonable* instead of *perfect* fits to the individual data.

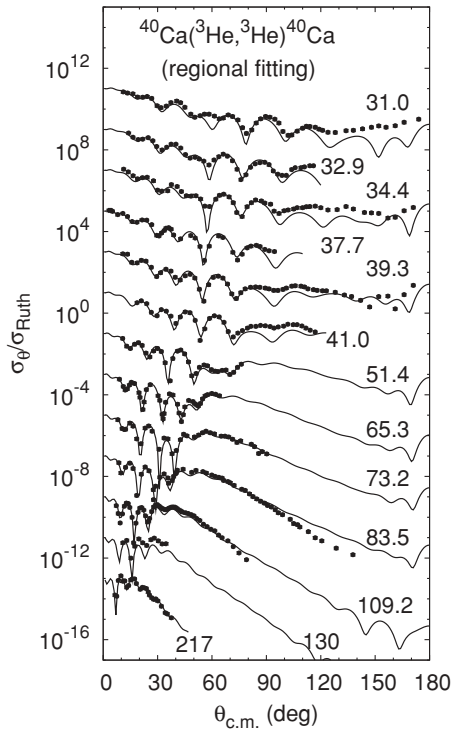

FIG. 21. Regional fitting of ^{3}He elastic scattering from a ^{40}Ca target. Compare this to the result of *global* fitting in Fig. 12.

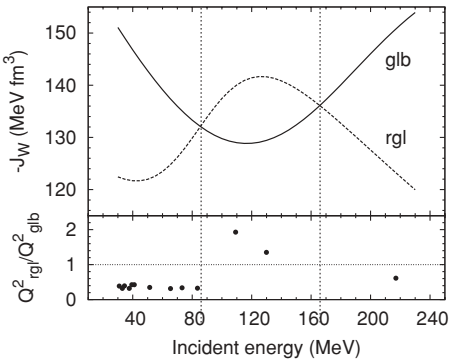

FIG. 22. Comparison between J_W of the ^{3}He-^{40}Ca potential from global fitting (labeled with "glb"; parameters in Table II) and regional fitting (labeled with "rgl"; parameters in Table IV) and their corresponding Q^2: $Q^2_{\rm glb}$ and $Q^2_{\rm rgl}$. As in Fig. 10, J_W is the sum of its surface and volume components. See the text for details.

B. Energy dependence of the real potential at low energies

We found that GDP08 tends to underestimate the differential cross sections at large angles for ^{3}He scattering from targets with $A_T \gtrsim 50$ when the incident energy is smaller than around 30 MeV. This is illustrated in Figs. 13 and 14. We also found that the fits for these energies can be improved by just reducing the depth of the real potentials of GDP08. These observations led us to study this problem by looking at the J_V value. Figure 23 depicts J_V as a function of the incident energy for ^{3}He elastic scattering from an ^{58}Ni target, where the points are results of individual fitting of the experimental data by Trost *et al.* [18] and the solid curve is calculated using the GDP08 global parameters. One can see that GDP08 is consistent with the individual fitting results rather well at higher energies down to around $E_{\rm inc} = 30$ MeV, but at low energies they are not consistent because for the latter J_V drops sharply as $E_{\rm inc}$ decreases. For the same target, this corresponds to a sharp drop of the depth parameter of the real potential with a decrease of the incident energy.

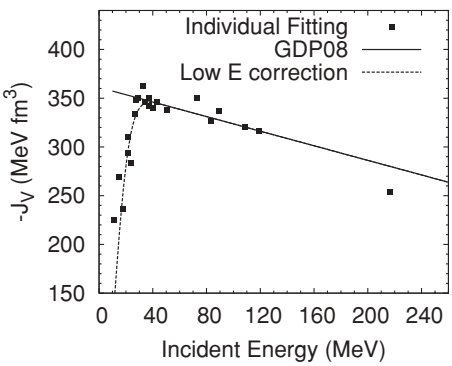

FIG. 23. J_V as a function of the incident energy for ^{3}He elastic scattering from ^{58}Ni. The solid curve represents the result of the GDP08 global potential and the dots are based on individual fittings of the experimental data by Trost *et al.* [18]. The dashed curve is the result of the correction for $E_{\rm inc} < 30$ MeV to the real potential of GDP08 by Eq. (22).

In fact, we found that the fitting of the experimental data at the $E_{\rm inc} < 30$ MeV for targets of $A_T \gtrsim 50$ could be improved by multiplying a low-energy correction function $[f(E_{\rm inc})]$ to the depth of the real potential of GDP08 $[V_r^{\rm GDP08}(E_{\rm inc})]$ while keeping all the other parameters unchanged:

$$V_r(E_{\rm inc}) = f(E_{\rm inc}) \times V_r^{\rm GDP08}(E_{\rm inc}),$$
$$f(E_{\rm inc}) = 1 - e^{(-E_{\rm inc}^2/\lambda)}. \quad (22)$$

Here $\lambda = 254.1 \pm 33.4$ MeV^2. This value of λ was obtained by simultaneous fitting of 131 sets of the ^{3}He scattering data in the range of $58 \leqslant A_T \leqslant 209$ and $12 \leqslant E_{\rm inc} \leqslant 217$ MeV with all the 15 parameters of GDP08 fixed. Note that here $V_r^{\rm GDP08} = V_0 + V_e \times (E_{\rm inc} - E_C)$. When applying the low-energy correction to the real potential of GDP08, as is shown by the dashed curve in Fig. 23, the results reported in Ref. [18] are very well reproduced at low energies. The relatively large discrepancy at 217 MeV may be related to the fact that the authors of Ref. [18] were only using surface imaginary potentials (W_s) in their individual fittings, whereas the result of GDP08 shows that it is the volume absorption (W_v) that dominates at this energy (see Fig. 10). Forcing the fitting of data using only W_s will certainly result in a real potential that does not follow the global behavior.

However, according to the work of Trost *et al.*, this additional factor might not be good for light targets because there is a transition in the form of energy dependence of the real potential depth from heavy to light targets (see Fig. 3 in Ref. [18]). A comparison with the experimental data shows that this energy correction function will degrade the prediction of ^{3}He-nucleus scattering at low energies for targets of $A_T \lesssim 50$ and has no advantage for ^{3}H-nucleus scattering at low energies for targets of $A_T \gtrsim 120$. We thus suggest using this low-energy correction function only for targets with $58 \lesssim A_T \lesssim 120$. We note that this is a rather preliminary result. A detailed study of the energy dependence of the optical potential for the $A = 3$ projectiles with the attempt to expand the simultaneous fit to the $E_{\rm inc} < 30$ MeV and/or $A_T < 40$ region by using different forms of energy and mass dependence of the global potential has not been completed yet.

C. Reduction factor of J_V

One of the major motivations for the study of the global potential for the $A = 3$ nuclei is to provide a benchmark for theories of elastic scattering, for example, the double-folding model. The real part of the ^{3}He-nucleus potential at a certain energy $E_{\rm inc}$ has been found to be shallower than the sum of nucleon-nucleus potentials at $E_{\rm inc}/3$ [18,39,65]. Theoretical work such as that of Perkin *et al.* attributed this to the internal motions of nucleons in the projectile, the three-body term, and the Pauli principle correction [120]. GDP08 allows us to do this comparison within a much larger energy range. For this purpose we define the following reduction factor of J_V for the volume integral of the real GDP08 global potential $[J_V^{\rm GDP08}(A_T, E_{\rm inc})]$ and that of the potential for $A = 3$ nuclei obtained by any other means $[J_V(A_T, E_{\rm inc})]$:

$$\eta^{J_V}(A_T, E_{\rm inc}) = \frac{J_V^{\rm GDP08}(A_T, E_{\rm inc})}{J_V(A_T, E_{\rm inc})}. \quad (23)$$

Obviously η^{J_V} is a function of A_T and $E_{\rm inc}$.

As an example, we calculate η^{J_V} as a function of the incident energy $E_{\rm inc}$ for ^{3}He on a ^{58}Ni target for (i) the double-folding potential, $\eta^{J_V}_{\rm DFP}$, and (ii) a superposition of the CH89 global potentials for protons (V_P) and neutrons (V_n) at $E_{\rm inc}^{(1/3)} = E_{\rm inc}/3$, $\eta^{J_V}_{\rm CH89}$, with

$$V_{\rm CH89}\left(E_{\rm inc}^{(1/3)}\right) = 2V_P\left(E_{\rm inc}^{(1/3)}\right) + V_n\left(E_{\rm inc}^{(1/3)}\right).$$

The double-folding calculations were described in Sec. II. The calculated volume integrals and reduction factors are shown in Fig. 24. One can see the following for the ^{3}He-^{58}Ni potential:

(i) For the reduction factor related to the CH89 global potential, $\eta^{J_V}_{\rm CH89}$, (i) $\eta^{J_V}_{\rm CH89}$ is around 0.8 when $E_{\rm inc}$ is less than around 120 MeV (40 MeV/nucleon), a result that is very consistent with the results in Ref. [120], and (ii) $\eta^{J_V}_{\rm CH89}$ increases with increasing incident energy. Theoretical results in Ref. [120] suggested that the reduction of J_V of the ^{3}He potential occurs mainly because of the internal motion of the nucleons in ^{3}He. If this theoretical model is correct, one would expect that the reduction should get smaller as the incident energy increases. The fact in Fig. 24 that $\eta^{J_V}_{\rm CH89}$ increases with increasing incident energy thus provides strong support for that theoretical model.

(ii) The volume integrals of the double-folding potentials are consistent with the GDP08 global potential within 20% in the energy range from 20 to 250 MeV.

(iii) The reduction factor related to the double-folding potential, $\eta^{J_V}_{\rm DFP}$, increases with increasing incident energy

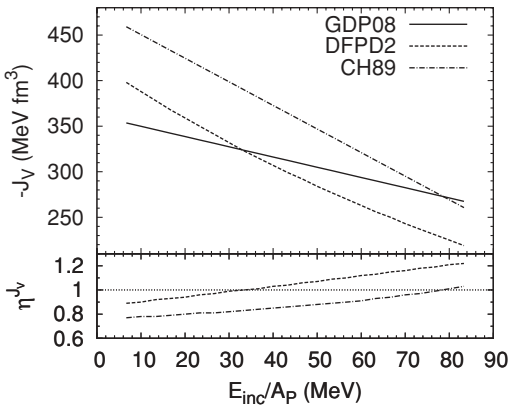

FIG. 24. (Upper panel) Comparison between volume integrals of the real potential of ^{3}He with ^{58}Ni target calculated by using (i) the GDP08 global potential (solid curve), (ii) double-folding model calculations (dashed curve), and (iii) the summation of the CH89 global proton and neutron potentials (dash-dotted curve). The energies have been scaled to $E_{\rm inc}/A_P$ with $A_P = 3$ for ^{3}He and $A_P = 1$ for protons and neutron. (Lower panel) Reduction factors of the volume integrals of the real potentials. The dashed and dash-dotted curves are for $\eta^{J_V}_{\rm DFPD2}$ and $\eta^{J_V}_{\rm CH89}$, respectively. See the text for details.

TABLE V. The spin-orbit potential parameters. These parameters were obtained by fitting the same sets of data as for GDP08 by fixing all the GDP08 parameters.

Parameter	Value	Uncertainty	Units		Correlation coefficients			
V_{so0}	1.7	1.6	MeV fm^2		V_{so0}	V_{soe}	r_{so}	$r_{so}^{(0)}$
V_{soe}	−0.02	0.02	fm^2	V_{soe}	−0.7			
r_{so}	0.64	0.29	fm	r_{so}	−0.1	−0.1		
$r_{so}^{(0)}$	1.18	0.86	fm	$r_{so}^{(0)}$	−0.2	0.1	−0.4	
a_{so}	0.13	0.58	fm	a_{so}	0.2	−0.1	−0.1	−0.1

and it is larger than 1.0 when E_{inc} is larger than 100 MeV. This may suggest some corrections to the effective nucleon-nucleon interaction used in the double-folding calculations.

D. The spin-orbit potential

As has been stated in Sec. III D, the spin-orbit potential was not included in the global fitting because its parameters were found to be not well defined by the experimental data included in the present analysis. We study the spin-orbit potential by fitting the same set of experimental data with all 15 GDP08 parameters fixed. We have found a set of spin-orbit potential parameters that is stable against the changes of their initial values. The values of the spin-orbit parameters, their uncertainties, and correlation coefficients are listed in Table V. Although the resulting parameters have quite large uncertainties, their values are consistent with previous studies [39,46,50,77]. Compared to the nucleon-nucleus potentials, V_{so} is around 1/3 of its counterpart in the CH89 potential [8] and all other nucleon-nucleus potentials cited in Ref. [10]. The diffuseness parameter a_{so} here is much smaller than those found for nucleon-nucleus potentials [8,10].

Previous studies [39,91] have shown that improvement of the description of elastic scattering data by including spin-orbit potentials is negligible and mainly at the backward angles, especially when $V_{so} \lessapprox 2$ MeV fm^2 [44]. It is true also in the present work. Figure 25 shows the Q^2_{so}/Q^2_{GDP08} value for each data set and their corresponding incident energies and target mass numbers, where Q^2_{so} are the Q^2 values calculated by including the spin-orbit potentials in Table V and Q^2_{GDP08} are the Q^2 values calculated with the GDP08 potential only. One can see that (i) for most data sets $0.9 < Q^2_{so}/Q^2_{GDP08} < 1.1$, which means that fittings of these data were not improved or only slightly improved by including the spin-orbit potential, and (ii) the data sets whose fittings were improved by including the spin-orbit potentials are mainly in the region of $A_T < 70$ and $E_{inc} < 80$ MeV. But in the same region, there are three data sets whose fittings were degraded when including these spin-orbit potentials. Note that these parameters cannot be used for incident energies larger than 85 MeV because V_{so} will be negative for these energies. Polarization data are necessary to study the global spin-orbit potential of the $A = 3$ projectiles and to reduce the uncertainties obtained in the present work.

E. Effect of Coulomb corrections to the incident energies

The Coulomb potentials experienced by ^{3}He and ^{3}H can have a difference as large as around 19 MeV for target ^{208}Pb. However, since the energy dependence factor of the real potential, V_e, is relatively small the effect of Coulomb corrections to the real potential is not important (less than around 2 MeV with respect to the total potential depth of around 110 MeV). It has larger effects in imaginary potentials. Figure 26 shows how the variations of the imaginary potentials,

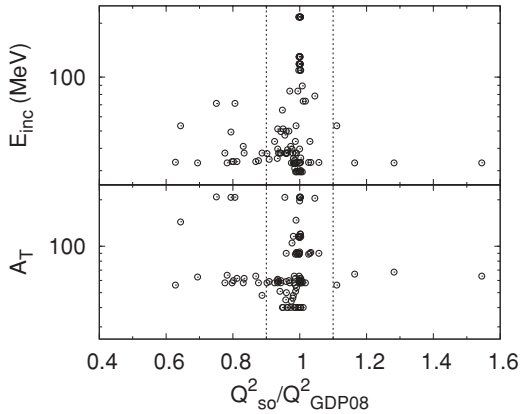

FIG. 25. Effect of spin-orbit potentials on the elastic scattering data viewed by Q^2. See the text for details.

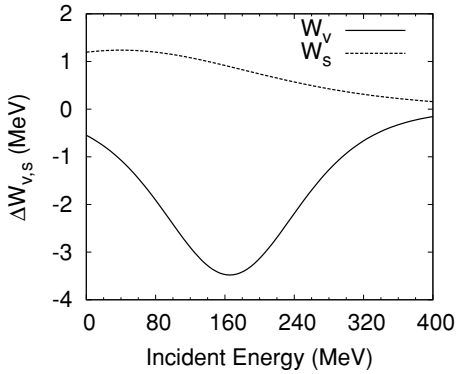

FIG. 26. Variation of W_v and W_s from Coulomb corrections as functions of incident energy. The GDP08 potential parameters were used here for an ^{3}H projectile with a ^{208}Pb target. See text for details.

ΔW_v and ΔW_s, depend on the incident energy. The projectile and target are ^{3}H and ^{208}Pb, respectively. ΔW_v and ΔW_s are defined as the differences between potentials calculated using the GDP08 parameters *with* and *without* taking into account the Coulomb corrections to the incident energies, for volume and surface imaginary potentials, W_v and W_s, respectively. One can see that the Coulomb corrections mainly affect the volume imaginary potential at around 170 MeV. The same is true for the ^{3}He projectile except that the values of ΔW_v and ΔW_s are larger. We thus study the effect of Coulomb corrections to the differential cross sections for ^{3}He elastic scattering from different targets at 130 MeV. The results are shown in Fig. 27. It is obvious that at the same incident energy the Coulomb correction effect increases with the increasing charge numbers of the targets and it manifests itself mainly at larger scattering angles.

Of course the Coulomb correction term only has meaning in the context of fitting elastic scattering data of both ^{3}He and ^{3}H projectiles simultaneously, which is not the case in the present work. However, we show in Fig. 28 that the Coulomb correction has some positive effects on the ^{3}H scattering as well. The case under study is ^{3}H elastic scattering from ^{208}Pb at 33 MeV [115]. From the solid curve one can see that with

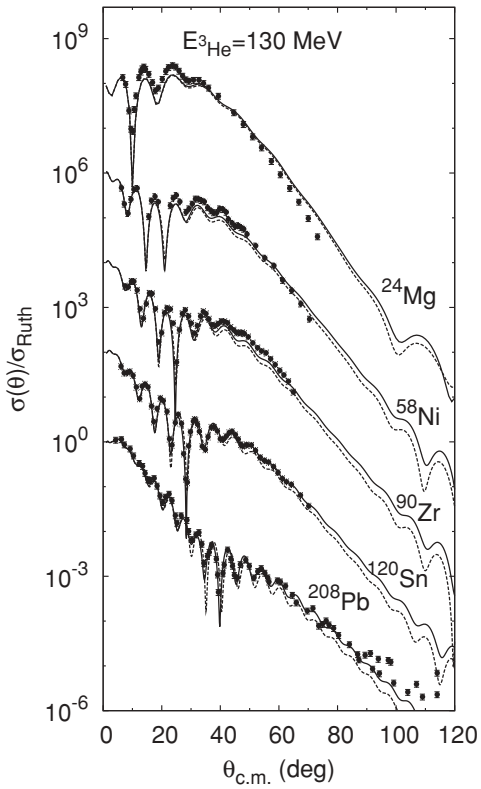

FIG. 27. Comparison between optical model calculations and experimental data of ^{3}He elastic scattering from different targets at an incident energy of 130 MeV [51,62]. The solid and dashed curves were calculated with and without Coulomb corrections to the incident energy, respectively, using the GDP08 potential parameters. See text for details.

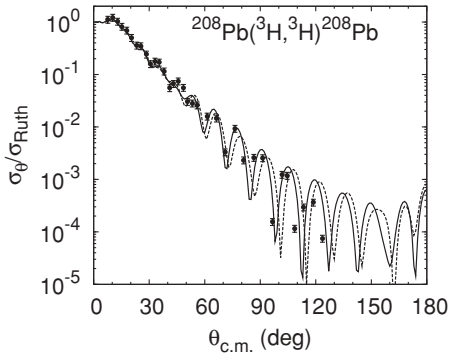

FIG. 28. Comparison between optical model calculations and experimental data of ^{3}H elastic scattering from ^{208}Pb at 33 MeV [115]. The solid and dashed curves were calculated with and without Coulomb corrections to the incident energy, respectively, using the GDP08 potential parameters.

the Coulomb correction taken into account the phase of the angular distribution is better reproduced. As has been shown in Fig. 26, the Coulomb correction effect for the ^{208}Pb target is most important for incident energies of around 170 MeV. Unfortunately, no experimental data at this region could be found for the ^{3}H projectile. We welcome measurements of ^{3}H elastic scattering at higher energies to test the GDP08 potential.

VI. CONCLUSIONS

In conclusion, a set of global optical potential parameters for ^{3}He-nucleus elastic scattering, GDP08, was obtained by simultaneously fitting 106 sets of ^{3}He-nucleus scattering data covering the range of $40 \leqslant A_T \leqslant 209$ in the target masses and $30 \leqslant E \leqslant 217$ MeV in the incident energy. This global potential is found to account for ^{3}H-nucleus elastic scattering as well, which makes it a global optical potential for $A = 3$ nuclei. Uncertainties and the correlation coefficients of the global parameters were also obtained by using the bootstrap method. We expect the GDP08 potential will be very useful to investigators making systematic studies of nuclear reactions involving ^{3}He or ^{3}H scattering from both stable targets and radioactive beams. We discussed the special behavior of the energy dependence of the ^{3}He-^{40}Ca potential, the energy dependence of the real potential at low energies for the $A_T \gtrsim 58$ nuclei, and the spin-orbit potential parameters. We also defined and calculated the reduction factor of the real part of GDP08 against the double-folding calculations and the CH89 nucleon-nucleus potential.

ACKNOWLEDGMENT

D. Y. Pang would like to thank his colleagues in Dubna, where this work was initiated, for their warm hospitality. Oak Ridge National Laboratory is managed by UT-Battelle, LLC under Contract DE-AC05-00OR22725 with the US Department of Energy.

[1] P. E. Hodgson, *The Optical Model of Elastic Scattering* (Clarendon, Oxford, 1963).
[2] N. Austern, *Direct Nuclear Reaction Theories* (Wiley, New York, 1970).
[3] G. R. Satchler, *Direct Nuclear Reactions* (Oxford University Press, New York, 1983).
[4] N. K. Glendenning, *Direct Nuclear Reactions* (World Scientific, Singapore, 2004).
[5] M. B. Tsang, J. Lee, and W. G. Lynch, Phys. Rev. Lett. **95**, 222501 (2005).
[6] J. Lee, M. B. Tsang, and W. G. Lynch, Phys. Rev. C **75**, 064320 (2007).
[7] A. J. Koning and J. P. Delaroche, Nucl. Phys. **A713**, 231 (2003).
[8] R. L. Varner, W. J. Thompson, T. L. McAbee, E. J. Ludwig, and T. B. Clegg, Phys. Rep. **201**, 57 (1991).
[9] F. G. Perey, Phys. Rev. **131**, 745 (1963).
[10] C. M. Perey and F. G. Perey, At. Data Nucl. Data Tables **17**, 1 (1976), and references herein.
[11] F. D. Becchetti Jr. and G. W. Greenlees, Phys. Rev. **182**, 1209 (1969).
[12] C. M. Perey and F. G. Perey, Phys. Rev. **132**, 755 (1963).
[13] W. W. Daehnick, J. D. Childs, and Z. Vrcelj, Phys. Rev. C **21**, 2253 (1980).
[14] F. D. Becchetti Jr. and G. W. Greenlees. in *Polarization Phenomena in Nuclear Reactions*, edited by H. H. Barschall and W. Haeberli (University of Wisconsin Press, Madison, 1971), p. 682.
[15] X. Li, C. Liang, and C. Cai, Nucl. Phys. **A789**, 103 (2007).
[16] M. Hyakutake, M. Matoba, I. Kumabe, M. Fukuda, T. Komatuzaki, T. Yamagata, M. Tanaka, M. Inoue, I. Miura, and H. Ogata, Nucl. Phys. **A311**, 161 (1978).
[17] M. Hyakutake, I. Kumabe, M. Fukada, T. Komatuzaki, T. Yamagata, M. Inoue, and H. Ogata, Nucl. Phys. **A333**, 1 (1980).
[18] H. J. Trost, P. Lezoch, and U. Strohbusch, Nucl. Phys. **A462**, 333 (1987).
[19] R. J. Eastgate, W. J. Thompson, and R. A. Hardekopf, Comput. Phys. Commun. **5**, 69 (1973).
[20] F. James and M. Roos, Comput. Phys. Commun. **10**, 343 (1975).
[21] J. Lee, D. Y. Pang, and M. B. Tsang (submitted to Phys. Rev. C).
[22] J. Vernotte, G. Berrier-Ronsin, J. Kalifa, R. Tamisier, and B. H. Wildenthal, Nucl. Phys. **A571**, 1 (1994).
[23] B. A. Brown, A. Etchegoyen, N. S. Godwin, W. D. M. Rae, W. A. Richter, W. E. Ormand, E. K. Warburton, J. S. Winfield, L. Zhao, and C. H. Zimmerman, MSU-NSCL Report No. 1289.
[24] D. T. Khoa and G. R. Satchler, Nucl. Phys. **A668**, 3 (2000).
[25] D. T. Khoa, G. R. Satchler, and W. von Oertzen, Phys. Rev. C **56**, 954 (1997).
[26] D. T. Khoa (private communication).
[27] J. Cook and R. J. Griffiths, Nucl. Phys. **A366**, 27 (1981).
[28] B. A. Brown, Phys. Rev. C **58**, 220 (1998).
[29] D. M. Patterson, R. R. Doering, and A. Galonsky, Nucl. Phys. **A263**, 261 (1976).
[30] P. P. Urone, L. W. Put, and B. W. Ridley, Nucl. Phys. **A186**, 344 (1972).
[31] J. Kamiya, K. Hatanaka, T. Adachi, K. Fujita, K. Hara, T. Kawabata, T. Noro, H. Sakaguchi, N. Sakamoto, Y. Sakemi, Y. Shimbara, Y. Shimizu, S. Terashima, M. Uchida, T. Wakasa, Y. Yasuda, H. P. Yoshida, and M. Yosoi, Phys. Rev. C **67**, 064612 (2003).
[32] H. Fujimura, H. Akimune, I. Daito, M. Fujiwara, K. Hara, K. Y. Hara, M. N. Harakeh, F. Ihara, T. Inomata, K. Ishibashi, T. Ishikawa, T. Kawabata, A. Tamii, M. Tanaka, H. Toyokawa, T. Yamanaka, and M. Yosoi, Phys. Rev. C **69**, 064327 (2004).
[33] http://www-nds.iaea.org/exfor/exfor00.htm.
[34] E. F. Gibson, B. W. Ridley, J. J. Kraushaar, and M. E. Rickey, Phys. Rev. **155**, 1194 (1967).
[35] H. H. Chang, B. W. Ridley, T. H. Braid, T. W. Conlon, E. F. Gibson, and N. S. P. King, Nucl. Phys. **A297**, 105 (1978).
[36] N. Nakanishi, Y. Chiba, Y. Awaya, and K. Matsuda, Nucl. Phys. **A140**, 417 (1970).
[37] A. Springer, M. Chabre, D. L. Hendrie, and H. G. Pugh, Phys. Lett. **20**, 397 (1966).
[38] S. L. Tabor, C. C. Chang, M. T. Collins, G. J. Wagner, J. R. Wu, D. W. Halderson, and F. Petrovich, Phys. Rev. C **25**, 1253 (1982).
[39] H.-J. Trost, A. Schwarz, U. Feindt, F. H. Heimlich, S. Heinzel, J. Hintze, F. Körber, R. Lekebusch, P. Lezoch, G. Möck, W. Paul, E. Roick, M. Wolfe, J. Worzeck, and U. Strohbusch, Nucl. Phys. **A337**, 377 (1980).
[40] N. Willis, I. Brissaud, Y. Le Bornec, B. Tatischeff, and G. Duhamel, Nucl. Phys. **A204**, 454 (1973).
[41] Y.-W. Lui, O. Karban, S. Roman, R. K. Bhowmik, J. M. Nelson, and E. C. Pollacco, Nucl. Phys. **A333**, 205 (1980).
[42] J. S. Hanspal, R. J. Griffiths, N. M. Clarke, J. M. Barnwell, O. Karban, and S. Roman, Nucl. Phys. **A427**, 297 (1984).
[43] R. W. Barnard and G. D. Jones, Nucl. Phys. **A111**, 17 (1968).
[44] P. P. Urone, L. W. Put, B. W. Ridley, and G. D. Jones, Nucl. Phys. **A167**, 383 (1971).
[45] J. W. Luetzelschwab and J. C. Hafele, Phys. Rev. **180**, 1023 (1969).
[46] A. Farooq, S. Roman, J. D. Brown, O. Karban, and G. Rai, Nucl. Phys. **A555**, 585 (1993).
[47] C. J. Marchese, R. J. Griffiths, N. M. Clarke, G. J. Pyle, G. T. A. Squier, and M. E. Cage, Nucl. Phys. **A191**, 627 (1972).
[48] C. J. Marchese, N. M. Clarke, and R. J. Griffiths, Nucl. Phys. **A202**, 421 (1973).
[49] C. R. Bingham and M. L. Halbert, Phys. Rev. **169**, 933 (1968).
[50] M. E. Cage, D. L. Clough, A. J. Cole, J. B. A. England, G. J. Pyle, P. M. Rolph, L. H. Watson, and D. H. Worledge, Nucl. Phys. **A183**, 449 (1972).
[51] A. Djaloeis, J.-P. Didelez, A. Galonsky, and W. Oelert, Nucl. Phys. **A306**, 221 (1978).
[52] T. Fujisawa, H. Kamitsubo, T. Wada, and M. Igarashi, J. Phys. Soc. Jpn. **27**, 278 (1969).
[53] R. H. Siemssen, T. H. Braid, D. Dehnhard, and B. Zeidman, Phys. Lett. **18**, 155 (1965).
[54] R. W. Barnard and G. D. Jones, Nucl. Phys. **A106**, 497 (1968).
[55] J. C. Hafele, C. B. Fulmer, and F. G. Kingston, Phys. Lett. **B31**, 17 (1970).
[56] C. B. Fulmer and J. C. Hafele, Phys. Rev. C **5**, 1969 (1972).
[57] S. M. Barr and R. M. Delvechio, Phys. Rev. C **15**, 114 (1977).
[58] P. D. Kunz, E. Rost, R. R. Johnson, G. D. Jones, and S. I. Hayakawa, Phys. Rev. **185**, 1528 (1969).
[59] P. B. Woollam, R. J. Griffiths, and N. M. Clarke, Nucl. Phys. **A189**, 321 (1972).
[60] R. Eagle, N. M. Clarke, R. J. Griffiths, C. B. Fulmer, and D. C. Hensley, J. Phys. G: Nucl. Part. Phys. **1**, 358 (1975).

[61] M. C. Radhakrishna, N. G. Puttaswamy, H. Nann, J. D. Brown, W. W. Jacobs, W. P. Jones, D. W. Miller, P. P. Singh, and E. J. Stephenson, Phys. Rev. C **37**, 66 (1988).
[62] N. Heberle, H. Clement, M. Ermer, P. Grabmayr, M. Hammans, R. Henneck, and I. Sick, Phys. Lett. **B250**, 15 (1990).
[63] W. C. Parkinson, D. L. Hendire, H. H. Duhm, J. Mahoney, J. Saundinos, and G. R. Satchler, Phys. Rev. **178**, 1976 (1969).
[64] C. B. Fulmer, J. C. Hafele, and N. M. Clarke, Phys. Rev. C **12**, 87 (1975).
[65] C. J. Marchese, N. M. Clarke, and R. J. Griffiths, Phys. Rev. Lett. **29**, 660 (1972).
[66] R. J. Griffiths, F. Duggan, and N. M. Clarke, J. Phys. G: Nucl. Part. Phys. **7**, 381 (1981).
[67] O. Kamigaito, H. Sakaguchi, M. Nakamura, S. Hirata, H. Togawa, T. Nakano, M. Yosoi, M. Ieiri, T. Ichihara, H. M. Shimizu, Y. Nakai, and S. Kobayashi, Phys. Rev. C **45**, 1533 (1992).
[68] P. E. Hodgson, *Nuclear Reactions and Nuclear Structure* (Clarendon, Oxford, 1971).
[69] B. Efron, Biometrika **68**, 589 (1981).
[70] B. Efron, SIAM Rev. **21**, 460 (1979).
[71] P. Diaconis and B. Efron, Sci. Am. **248**, 116 (1983).
[72] I. J. Thompson, Comput. Phys. Rep. **7**, 3 (1988).
[73] H. Lüdecke, W.-T. Tan, H. Werner, and J. Zimmerer, Nucl. Phys. **A109**, 676 (1968).
[74] R. W. Givens and M. K. Brussel, Nucl. Phys. **A187**, 490 (1972).
[75] J. Y. Park, J. L. Duggan, P. D. Miller, M. M. Duncan, and R. L. Dangle, Nucl. Phys. **A134**, 277 (1969).
[76] A. J. Buffa Jr. and M. K. Brussel, Nucl. Phys. **A195**, 545 (1972).
[77] W. E. Burcham, J. B. A. England, R. G. Harris, O. Karban, and S. Roman, Nucl. Phys. **A246**, 269 (1975).
[78] R. Görgen, F. Hinterberger, R. Jahn, P. Von Rossen, and B. Schüller, Nucl. Phys. **A320**, 296 (1979).
[79] G. Scheklinski, U. Strohbusch, and B. Goel, Nucl. Phys. **A153**, 97 (1970).
[80] W. S. McEver, T. B. Clegg, J. M. Joyce, E. J. Ludwig, and R. L. Walter, Phys. Rev. Lett. **24**, 1123 (1970).
[81] G. C. Ball and J. Cerny, Phys. Rev. **177**, 1466 (1969).
[82] A. S. Dem'yanova, E. F. Svinareva, S. A. Goncharov, S. N. Ershov, F. A. Gareev, G. S. Kazacha, A. A. Ogloblin, and J. S. Vaagen, Nucl. Phys. **A542**, 208 (1992).
[83] J. L. Yntema, B. Zeidman, and R. H. Bassel, Phys. Lett. **11**, 302 (1964).
[84] H. Kattenborn, C. Mayer-Böricke, and B. Mertens, Nucl. Phys. **A119**, 559 (1968).
[85] R. J. Griffiths, Nucl. Phys. **A102**, 329 (1967).
[86] H. H. Duhm, Nucl. Phys. **A118**, 563 (1968).
[87] K. H. Bray, J. Nurzyński, and G. R. Satchler, Nucl. Phys. **67**, 417 (1965).
[88] D. J. Baugh, G. J. B. Pyle, P. M. Rolph, and S. M. Scarrott, Nucl. Phys. **A95**, 115 (1967).
[89] D. Cline, W. Parker Alford, and L. M. Blau, Nucl. Phys. **73**, 33 (1965).
[90] K. M. Abdo, M. A. Abdulmomen, and J. D. Fox, Nucl. Phys. **A456**, 457 (1986).
[91] P. P. Urone, L. W. Put, H. H. Chang, and B. W. Ridley, Nucl. Phys. **A163**, 225 (1971).
[92] D. E. Rundquist, M. K. Brussel, and A. I. Yavin, Phys. Rev. **168**, 1287 (1968).
[93] M. Conjeaud, S. Harar, and Y. Cassagnou, Nucl. Phys. **A117**, 449 (1968).
[94] A. Ingemarsson, G. J. Arendse, A. Auce, R. F. Carlson, A. A. Cowley, A. J. Cox, S. V. Förtsch, R. Johansson, B. R. Karlson, M. Lantz, J. Peavy, J. A. Stander, G. F. Steyn, and G. Tibell, Nucl. Phys. **A696**, 3 (2001).
[95] P. E. Hodgson, in Proceedings of the Specialists' Meeting on the Nucleon Nucleus Optical Model up to 200 MeV, 13–15 November 1996, Bruyères-le-Chatel, France, http://db.nea.fr/html/science/om200/.
[96] T. Yamagata, H. Utsunomiya, M. Tanaka, S. Nakayama, N. Koori, A. Tamii, Y. Fujita, K. Katori, M. Inoue, M. Fujiwara, and H. Ogata, Nucl. Phys. **A589**, 425 (1995).
[97] J. Raynal, ECIS03 code (distributed by NEA DATA BANK).
[98] P. A. Schmelzbach, R. A. Hardekopf, R. F. Haglund, and G. G. Ohlsen, Phys. Rev. C **17**, 16 (1978).
[99] J. D. Garrett and O. Hansen, Nucl. Phys. **A212**, 600 (1973).
[100] J. C. Hafele, E. R. Flynn, and A. G. Blair, Phys. Rev. **155**, 1238 (1967).
[101] R. A. Hardekopf, L. R. Veeser, and P. W. Keaton Jr., Phys. Rev. Lett. **35**, 1623 (1975).
[102] J. D. Knight, C. J. Orth, W. T. Leland, and A. B. Tucker, Phys. Rev. C **9**, 1467 (1974).
[103] R. C. Ragaini, J. D. Knight, and W. T. Leland, Phys. Rev. C **2**, 1020 (1970).
[104] A. B. Tucker, K. E. Apt, J. D. Knight, and C. J. Orth, Phys. Rev. C **6**, 2075 (1972).
[105] T. J. Mulligan, E. R. Flynn, O. Hansen, R. F. Casten, and R. K. Sheline, Phys. Rev. C **6**, 1802 (1972).
[106] J. D. Sherman, E. R. Flynn, N. Stein, J. W. Sunier, and D. G. Burke, Phys. Rev. C **13**, 2122 (1976).
[107] J. S. Hanspal, K. I. Pearce, N. M. Clarke, R. J. Griffiths, R. E. Brown, R. A. Hardekopf, and W. Grüebler, Nucl. Phys. **A455**, 494 (1986).
[108] J. M. Barnwell, R. J. Griffiths, R. E. Brown, R. A. Hardekopf, N. Jarmie, and F. D. Correll, Nucl. Phys. **A388**, 542 (1982).
[109] R. A. Hardekopf, R. F. Haglund, G. G. Ohlsen, W. J. Thompson, and L. R. Veeser, Phys. Rev. C **21**, 906 (1980).
[110] P. Schwandt, R. E. Brown, F. D. Correll, R. A. Hardekopf, and G. G. Ohlsen, Phys. Rev. C **26**, 369 (1982).
[111] P. W. Keaton Jr., D. D. Armstrong, L. R. Veeser, H. T. Fortune, and N. R. Roberson, Nucl. Phys. **A179**, 561 (1972).
[112] A. S. Dem'yanova, H. G. Bohlen, B. Gebauer, S. A. Goncharov, A. A. Korsheninnikov, Ch. Langner, M. von Lucke-Petsch, W. von Oertzen, A. A. Ogloblin, O. Ya. Osadchy, A. N. Ostrowski, M. Wilpert, and Th. Wilpert, Nucl. Phys. **A553**, 727c (1993).
[113] E. R. Flynn, D. D. Armstrong, J. G. Beery, and A. G. Blair, Phys. Rev. **182**, 1113 (1969).
[114] G. J. Igo, P. D. Barnes, E. R. Flynn, and D. D. Armstrong, Phys. Rev. **177**, 1831 (1969).
[115] J. B. A. England, L. Zybert, G. T. A. Squier, O. Karban, R. Zybert, J. M. Nelson, D. Barker, B. R. Fulton, M. C. Mannion, C. A. Ogilvie, L. Potvin, C. Pinder, C. O. Blyth, G. C. Morrison, G. J. Pyle, S. Roman, N. M. Clarke, K. I. Pearce, P. J. Simmonds, R. J. Griffiths, D. L. Watson, M. D. Cohler, R. Wadsworth, J. O'Donnell, and M. Smithson, Nucl. Phys. **A475**, 422 (1987).
[116] P. R. Hayes, N. M. Clarke, K. I. Pearce, M. B. Becha, R. S. Mackintosh, J. B. A. England, L. Zybert, G. M. Field, and S. Roman, Nucl. Phys. **A540**, 171 (1992).

[117] K. I. Pearce, N. M. Clarke, R. J. Griffiths, P. J. Simmonds, A. C. Dodd, D. Barker, J. B. A. England, M. C. Mannion, and C. A. Ogilvie, J. Phys. G: Nucl. Part. Phys. **12**, 979 (1986).
[118] P. J. Simmonds, K. I. Pearce, P. R. Hayes, N. M. Clarice, R. J. Griffiths, M. C. Mannion, and C. A. Ogilvie, Nucl. Phys. **A482**, 653 (1988).
[119] Q. Shen, Nucl. Sci. Eng. **141**, 78 (2002).
[120] D. G. Perkin, A. M. Kobos, and J. R. Cook, Nucl. Phys. **A245**, 343 (1975).